

Metallic Nanoclusters

16

CHAPTER OUTLINE

| | |
|--|-----|
| 16.1 Introduction | 528 |
| 16.1.1 Nanoscience and Nanoclusters | 528 |
| 16.1.2 Liquid Drop Model | 528 |
| 16.1.3 Size and Surface/Volume Ratio | 528 |
| 16.1.4 Geometric and Electronic Shell Structures | 530 |
| 16.2 Electronic Shell Structure | 531 |
| 16.2.1 Spherical Jellium Model (<i>Phenomenological</i>) | 531 |
| 16.2.2 Self-Consistent Spherical Jellium Model | 532 |
| 16.2.3 Ellipsoidal Shell Model | 535 |
| 16.2.4 Nonalkali Clusters | 535 |
| 16.2.5 Large Clusters | 535 |
| 16.3 Geometric Shell Structure | 537 |
| 16.3.1 Close-Packing | 537 |
| 16.3.2 Wulff Construction | 537 |
| 16.3.3 Polyhedra | 538 |
| 16.3.4 Filling between Complete Shells | 540 |
| 16.4 Cluster Growth on Surfaces | 540 |
| 16.4.1 Monte Carlo Simulations | 540 |
| 16.4.2 Mean-Field Rate Equations | 541 |
| 16.5 Structure of Isolated Clusters | 542 |
| 16.5.1 Theoretical Models | 542 |
| 16.5.2 Structure of Some Isolated Clusters | 546 |
| 16.6 Magnetism in Clusters | 547 |
| 16.6.1 Magnetism in Isolated Clusters | 547 |
| 16.6.2 Experimental Techniques for Studying Cluster Magnetism | 549 |
| 16.6.3 Magnetism in Embedded Clusters | 553 |
| 16.6.4 Graphite Surfaces | 555 |
| 16.6.5 Study of Clusters by Scanning Tunneling Microscope | 555 |
| 16.6.6 Clusters Embedded in a Matrix | 557 |
| 16.7 Superconducting State of Nanoclusters | 558 |
| 16.7.1 Qualitative Analysis | 558 |
| 16.7.2 Thermodynamic Green's Function Formalism for Nanoclusters | 559 |
| Problems | 562 |
| References | 565 |

16.1 INTRODUCTION

16.1.1 Nanoscience and Nanoclusters

Nano objects have a size that is intermediate between atoms or molecules and bulk matter. The recent invention of a variety of tools for studying systems at the atomic level, coupled with the development of techniques for producing nanoclusters, has led to the use of nanoscience as a new field of study. The scanning probe microscopes (the first of which was the scanning tunneling microscope, or STM), make it possible to “see” individual atoms and molecules on surfaces of materials as well as to move them on the nanoscale.

New sources to produce clusters in the gas phase were developed in the 1960s and 1970s, but it was in 1980s that Knight et al.¹⁶ first produced clusters of alkali metals with approximately 100 atoms and systematically studied their properties. Nanoclusters can now be formed from most elements of the periodic table. They can be classified as metallic, semiconductor, ionic, rare gas, or molecular, according to their constituents. Clusters are classified as homogeneous if they contain a single type of atom or heterogeneous if they comprise more than one constituent. They may be neutral or charged (anions or cations). There have been two main approaches in creating nanostructures: top-down and bottom-up. In the top-down method, starting from a large piece of material, a nanostructure is formed by removing material from it through etching or machining by using an electron beam or focused ion beam lithography. In the bottom-up approach, nanoparticles or molecules are produced by chemical synthesis followed by ordered structures by physical or chemical interactions between the units. In this chapter, we will concentrate on the study of metallic nanoclusters.

16.1.2 Liquid Drop Model

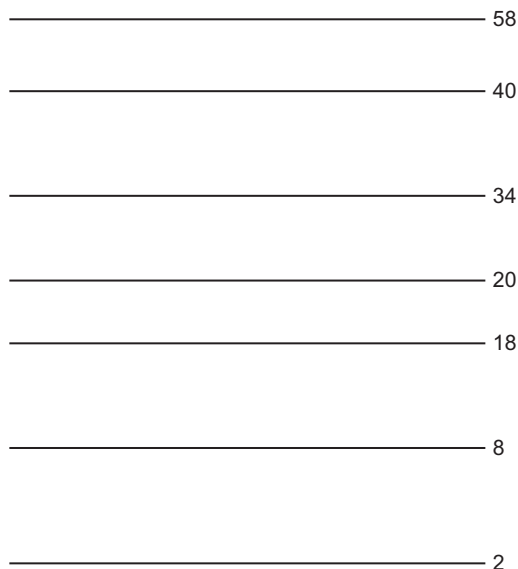
The simplest description of a metallic nanocluster is the liquid drop model (LDM). The cluster is represented as a sphere of radius R , which is related to the number of atoms N through the Wigner–Seitz radius r_s ,

$$R = N^{1/3} r_s. \quad (16.1)$$

Here, the Wigner–Seitz radius r_s , originally defined as the radius of the volume occupied by each valence electron, is equivalent to the volume occupied by each atom in a monovalent nanometal. The internal structure of the cluster is ignored in this model. This model is equivalent to the free electron theory of solids. However, the solid box has macroscopic dimensions with a continuum of energy levels, whereas the cluster box is a nanoscale entity and the energy levels are discrete. The first few energy levels for noninteracting electrons in a spherical box and the number of electrons required for complete filling of the shells are shown in Figure 16.1.

16.1.3 Size and Surface/Volume Ratio

The fraction of atoms that are on the surface of a cluster distinguishes the difference of the properties of the cluster from the bulk. One simple way to analyze this is to cut a regularly shaped object

**FIGURE 16.1**

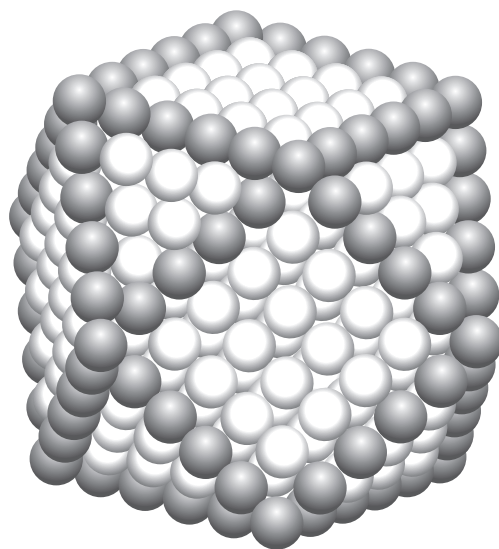
First few energy levels for noninteracting electrons in a spherical box.

from a fcc lattice and count the surface atoms for different size clusters. Such clusters have eight triangular and six square faces, as shown in Figure 16.2. The fraction of atoms that are on the surfaces of the clusters is shown in Figure 16.3.

Clusters represent a state of matter that is intermediate between atoms and the solid or liquid state, with properties that depend on the size, shape, and material of the particle. The arbitrary property per atom, $x(N)$, can be expressed as

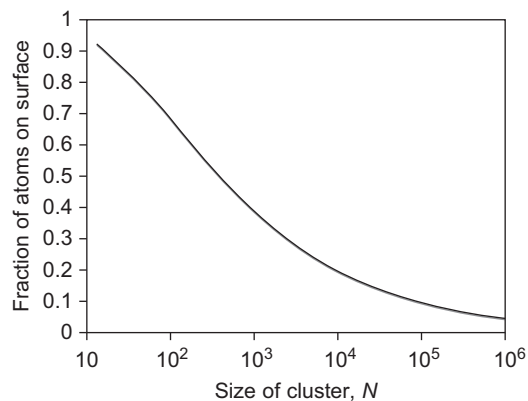
$$x(N) = a + bN^{-1/3}, \quad (16.2)$$

where the first term is the “bulk” contribution, and the second term is the “surface” contribution.

**FIGURE 16.2**

A 561-atom cut from a cuboctahedral cluster cut from a bulk fcc crystal.

Reproduced from Misra²⁸ with the permission of Elsevier.

**FIGURE 16.3**

Fraction of atoms on cuboctahedral clusters of N atoms.

Reproduced from Misra²⁸ with the permission of Elsevier.

16.1.4 Geometric and Electronic Shell Structures

Knight et al.¹⁶ produced clusters through the supersonic expansion of a metal/carrier gas mixture. The alkali metal is first vaporized and then seeded in the inert carrier gas (typically argon). The supersonic expansion of the mixture results in adiabatic cooling. The cluster is then ionized and passed through a mass spectrometer. Knight et al.¹⁶ observed marked peaks in the mass spectrum of the clusters indicating high stability at particular sizes. Their experiment results are reproduced in Figure 16.4.

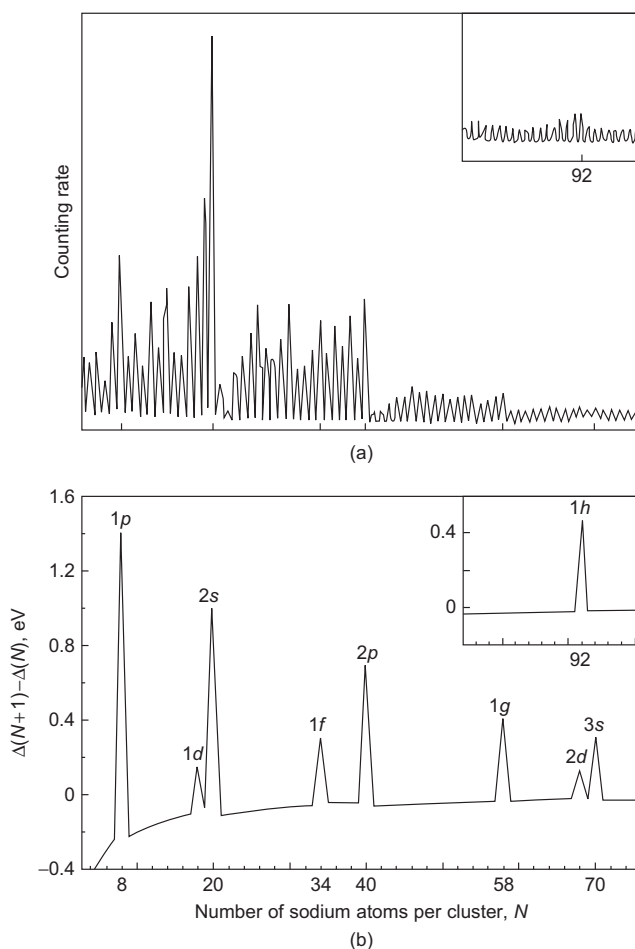


FIGURE 16.4

(a) The mass spectrum of sodium clusters with $N=4$ –75 and 75–100 (inset). (b) The calculated change in the electronic energy difference, $\Delta(N+1) - \Delta(N)$ versus N . The peak labeling corresponds to closed-shell orbitals.

Reproduced from Knight et al.¹⁶ with the permission of the American Physical Society.

The marked peaks or steps at special numbers in the sodium-cluster mass spectra are called “magic numbers.” These magic numbers were associated with complete filling of electronic shells, a concept of the electronic shell model borrowed from nuclear physics. From Figure 16.4, the magic number peaks are seen at cluster sizes $N = 8, 20, 40, 58, \text{ and } 92$.

16.2 ELECTRONIC SHELL STRUCTURE

16.2.1 Spherical Jellium Model (*Phenomenological*)

In the spherical jellium model, the ionic cores are replaced by a uniform positive charge background of radius R . The electrons are treated as independent particles moving in a parametrized phenomenological potential. The basic parameter of the model is the Wigner–Seitz radius r_s defined in Eq. (16.1). Further, the wave function for a spherically symmetric potential can be written as

$$\psi_{nlm}(\mathbf{r}) = R_{nl}(r)Y_{lm}(\theta, \phi). \quad (16.3)$$

There are three empirical potentials used to describe the nanoclusters, all borrowed from basic ideas of nuclear physics. The simplest model is the harmonic oscillator potential.

Harmonic Oscillator Potential

The harmonic oscillator potential is described by

$$V(r) = \frac{1}{2}m\omega_0 r^2. \quad (16.4)$$

The energy of the harmonic oscillator potential is given by

$$E_\nu = \left(\frac{3}{2} + \nu\right)\hbar\omega_0. \quad (16.5)$$

The quantum numbers (n, l) can be used for any spherically symmetric potential. Thus, all orbitals with the same value of $(2n + l)$ are degenerate and the energies are written in terms of the single quantum number $(2\nu + l - 2)$. The potential energy due to the background charge is

$$V(r) = \begin{cases} \frac{3e^2N}{8\pi\epsilon_0R^3} \left(\frac{r^2}{3} - R^2\right) & \text{if } r < R, \\ \frac{e^2Z}{4\pi\epsilon_0r} & \text{if } r > R. \end{cases} \quad (16.6)$$

So the harmonic oscillator potential mimics the potential felt by the electrons inside the cluster, provided the electron–electron interaction is ignored.

Spherical Square-Well Potential

The spherical square-well potential is described by

$$V(r) = \begin{cases} C & \text{for } r < R, \\ \infty & \text{otherwise.} \end{cases} \quad (16.7)$$

Here, C is a constant. The radial wave function $R_{nl}(r)$ for the square-well potential is written in terms of the spherical Bessel function $j_l(\kappa_{nl}R)$, where

$$\kappa_{nl} = \left[\frac{2m|E|}{\hbar^2} \right]^{1/2}. \quad (16.8)$$

The energy levels are determined by the boundary conditions $j_l(\kappa_{nl}R) = 0$ and, for each l , the first zero of j_l is given the quantum number $n = 1$, the second $n = 2$, and so on. The order of the energy levels (which are borrowed from nuclear physics and are different from atomic physics) are 1s, 1p, 1d, 2s, 1f, 2p, 1g, 2d, and so on. If two solutions have the same number of radial nodes, the one with higher l has higher energy. In this notation, the principal quantum number in atomic physics is equal to $n + l$. The interior of the jellium cluster will be electrically neutral if one includes the exchange-correlation contribution to the electrostatic potential of the electrons, and the effective potential will be nearly constant. The square-well potential essentially represents this phenomenon.

Woods–Saxon Potential

The Woods–Saxon potential $U(r)$ yields a better phenomenological representation of a potential that is flat in the middle of the cluster and rounded at the edges. This potential is described by

$$U(r) = \frac{-U_0}{\exp[(r-R)/\epsilon] + 1}. \quad (16.9)$$

U_0 is the sum of the Fermi energy and the work function of the bulk metal. R is determined by Eq. (16.4) with r_s , the Wigner-Seitz radius of the bulk. The parameter ϵ is taken to match the variation in the potential at the surface. This potential is flat in the middle of the cluster but rounded at the edges. The three potentials are shown in Figure 16.5.

In Figure 16.5, the degeneracy of the states of the Woods–Saxon potential is similar to that of the square-well potential, but the ordering of the energy levels is different. Knight et al.¹⁶ used the Woods–Saxon potential (Ref. 35) in the analysis of the mass spectra shown in Figure 16.3. The ordering of the energy levels is shown, and the cumulative totals of electrons are indicated above the energy levels. At the bottom of the figures are sketches of the potentials as a function of r .

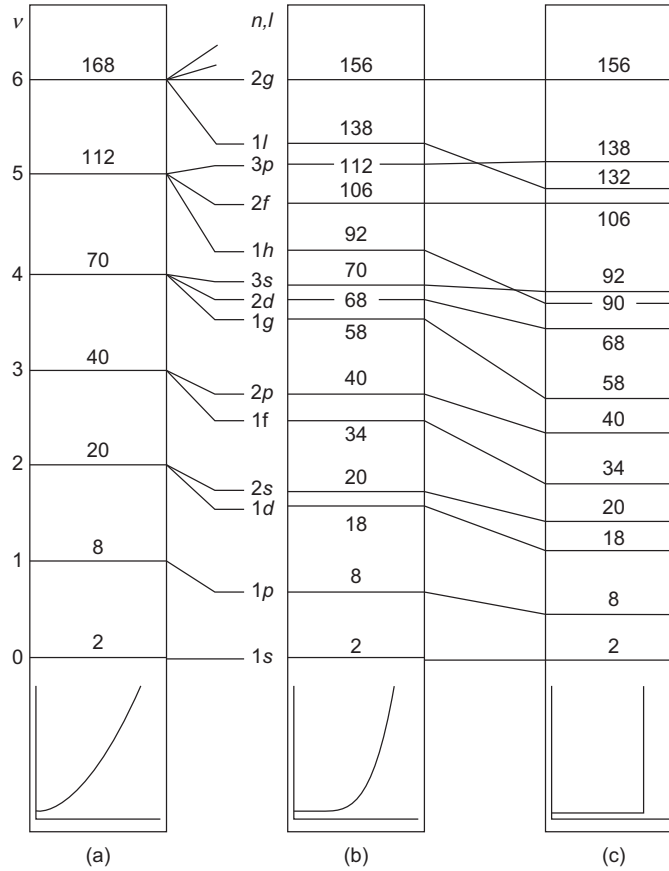
16.2.2 Self-Consistent Spherical Jellium Model

For an interacting electron gas, the density functional theory (DFT) based on the Hohenberg–Kohn (HK) theorem (discussed in detail in Section 7.8.1) is used. The basic assumption of DFT is that the total energy of the system is a functional of the electron density $n(\mathbf{r})$. The HK theorem states that the exact ground-state energy of a correlated electron system is a functional of the density, and the minimum is the ground-state density. One can apply the HK theorem to clusters. The density $n_I(r)$ of the smeared-out positive charge of the ions can be expressed as

$$n_I(r) = n_0 \theta(r - R), \quad (16.10)$$

where R is the cluster radius given in Eq. (16.1), θ is a step function, and n_0 is the constant bulk density of the metal

$$n_0 = \left(\frac{4\pi r_s}{3} \right)^{-1}. \quad (16.11)$$


FIGURE 16.5

Comparison of the (a) harmonic, (b) Woods–Saxon, and (c) square-well potentials.

Reproduced from Misra²⁸ with the permission of Elsevier.

The total energy can be written as

$$E[n] = E_{es}[n] + E_{ex}[n], \quad (16.12)$$

where $E_k[n]$ is the kinetic energy of a system of independent particles of density n ,

$$E_k[n] = \sum_i \frac{\hbar^2}{2m} |\nabla \psi_i|^2. \quad (16.13)$$

where $E_{es}[n]$ is the electrostatic energy,

$$E_{es}[n] = \frac{e^2}{2} \iint d\mathbf{r}' d\mathbf{r} \frac{[n(\mathbf{r}) - n_l(\mathbf{r})][n(\mathbf{r}') - n_l(\mathbf{r}')]}{|\mathbf{r} - \mathbf{r}'|}. \quad (16.14)$$

Following the procedure outlined in Section 7.8.2 (Ref. 17) (subject to the modification for a metallic cluster), we obtain (Problem 16.1)

$$-\frac{\hbar^2}{2m}\nabla^2\psi_i(\mathbf{r}) + V_{KS}(\mathbf{r})\psi_i(\mathbf{r}) = \varepsilon_i\psi_i(\mathbf{r}), \quad (16.15)$$

where

$$V_{KS}(\mathbf{r}) = V_H(\mathbf{r}) + V_{xc}(\mathbf{r}) \quad (16.16)$$

and

$$V_H(\mathbf{r}) = 2e^2 \int d\mathbf{r}' \frac{n(\mathbf{r}') - n(\mathbf{r}')}{|\mathbf{r} - \mathbf{r}'|}. \quad (16.17)$$

The local density approximation assumes that $n(\mathbf{r})$ is slowly varying. The exchange-correlation part of the total energy can be written as

$$E_{xc}[n] = \int d\mathbf{r} n(\mathbf{r}) \varepsilon_{xc}(n(\mathbf{r})), \quad (16.18)$$

and

$$V_{xc}(\mathbf{r}) = \frac{\partial \varepsilon_{xc}(n)}{\partial n} + \varepsilon_{xc}(n). \quad (16.19)$$

Here, $\varepsilon_{xc}(n)$ is the exchange and correlation energy of a uniform electron gas of density n .

A number of functional forms are used for ε_{xc} . The form used most often is given by Ekardt,⁷

$$\varepsilon_{xc}(n(\mathbf{r})) = -\frac{0.916}{r_s(\mathbf{r})} - 0.0666G(x(\mathbf{r})). \quad (16.20)$$

The first term is the exchange part, where

$$r_s(\mathbf{r}) = [3/4\pi n(\mathbf{r})]^{1/3}, \quad (16.21)$$

and the second term is the correlation part, where

$$G(x) = (1+x^3) \ln \left[1 + \frac{1}{x} \right] - x^2 + \frac{x}{2} - \frac{1}{3} \quad (16.22)$$

and

$$x(\mathbf{r}) = r_s(\mathbf{r})/11.4. \quad (16.23)$$

The wave functions and hence the energy are obtained self-consistently from the Kohn–Sham equations (Ref. 17). The Kohn–Sham potentials are fairly flat in the center of the cluster and analogous to the Woods–Saxon potential discussed earlier.

Due to the absence of the ionic structure, the simple jellium model, which works reasonably well for alkali metals, does not work out for higher-density materials such as aluminum. Recently,

in the “stabilized jellium model,” the ionic pseudopotentials have been introduced through a modified exchange-correlation potential.

16.2.3 Ellipsoidal Shell Model

The use of spheres is a justified approximation only for closed-shell structures. However, for open-shell structures, the ellipsoidal shell model (borrowed from nuclear physics) is used. The model is based on the harmonic oscillator Hamiltonian

$$H = \frac{p^2}{2m} + \frac{1}{2}m\omega_0^2 \left[\Omega_\perp^2(x^2 + y^2) + \Omega_z^2 z^2 \right] - U\hbar\omega_0[l^2 - \langle l^2 \rangle_n]. \quad (16.24)$$

It is essentially a spheroid that has two equal axes (x and y) and one unequal axis (z). Constant volume is maintained by imposing the condition $\Omega_\perp^2 \Omega_z = 1$, and the distortion is expressed by a parameter δ ,

$$\delta = \frac{2(\Omega_\perp - \Omega_z)}{\Omega_\perp + \Omega_z}. \quad (16.25)$$

The last term in Eq. (16.24) is an empirical addition that splits the states of different angular momenta and gives the same ordering as the Woods–Saxon potential. The potential is elongated in the x and y directions, and the cluster is elongated in the z -axis (prolate distortion), but when δ is negative, there is oblate distortion as well as expansion in the x - y plane. In Eq. (16.24), $\langle l^2 \rangle_n = (\frac{1}{2})n(n+3)$ (Problem 16.2).

One can obtain the wave function self-consistently from the Kohn–Sham equation outlined earlier. The wave functions are characterized by the quantum numbers (n, n_3, Λ) , where Λ is the component of \mathbf{l} along z , and n, n_1, n_2, n_3 are defined in Problem 16.3. Shell filling occurs with a prolate distortion until half-filling and then reverts to oblate. Closed-shell clusters are spherical, but there are subshell closings that are ellipsoidal.

16.2.4 Nonalkali Clusters

The noble metals (Cu, Ag, and Au) lie at the end of the $3d, 4d$, and $5d$ periods, respectively, with a filled d -shell of 10 electrons and a single valence electron. In bulk, the d -band falls well below the Fermi level, and the valence electrons are expected to behave similarly to that observed in alkali metal clusters. In the experiments of Katakuse et al.,¹⁵ the clusters were created as positively charged ions, so the number of electrons in a cluster was $N - 1$, and the magic numbers corresponding to electronic shell charges had fair agreement with experimental results. The electronic shell model also applies to divalent metals where $2N$ corresponds to the shell-filling numbers shown in Figure 16.4, leading to magic numbers at $N = 4, 9, 10, 17, 20, 29, 34, 35, 46, 53, 56, \dots$. This is also experimentally confirmed by another experiment by Katakuse et al.¹⁵

16.2.5 Large Clusters

The mass spectra of sodium clusters have been recorded up to sizes of about 25,000 atoms, in which the magic numbers are evident. However, the electronic energy levels of large clusters tend

to bunch together in groups so that there is a series of approximately degenerate levels (shells). From experimental results, it is apparent that these shells fill on a scale that is proportional to $N^{1/3}$. One can gain useful insight by considering the electronic shells that occur for potentials for which exact degeneracy occurs and for which there is an analytic solution.

We consider the harmonic oscillator potential and the energy-level scheme shown in Figure 16.5 and define a shell index K ($= \nu$ in Figure 16.5). If the states are labeled as (n, l) , all states with $K = 2n + l$ are degenerate. If $N(K)$ denotes the number of atoms in a cluster with complete levels filling up to and including the shell K ($K = 0, 1, 2, \dots$),

$$N(K) = \frac{1}{3}(K+1)(K+2)(K+3) \rightarrow \frac{K^3}{3}. \quad (16.26)$$

The shell index associated with the magic numbers is plotted against $N^{1/3}$ in Figure 16.6.

If all states are degenerate ($1/r$ potential), $K = n + l$ are degenerate. (The notation n_{at} in atomic physics is $n_{at} = n + l$). The number of states for a complete filling up to shell K is

$$N(K) = \frac{2}{3}K\left(K + \frac{1}{2}\right)(K+1) \rightarrow \frac{2}{3}K^3. \quad (16.27)$$

Thus, the general filling scale is $K \propto N^{1/3}$. Figure 16.6 shows the shell index K plotted against $N^{1/3}$.

Figure 16.6 distinctly shows that there is a break in behavior at about $N \approx 1500$. For $N < 1500$, the electronic shell model yields satisfactory results. However, for $N > 1500$, one has to use a different model. The model used is known as the geometric shell model.

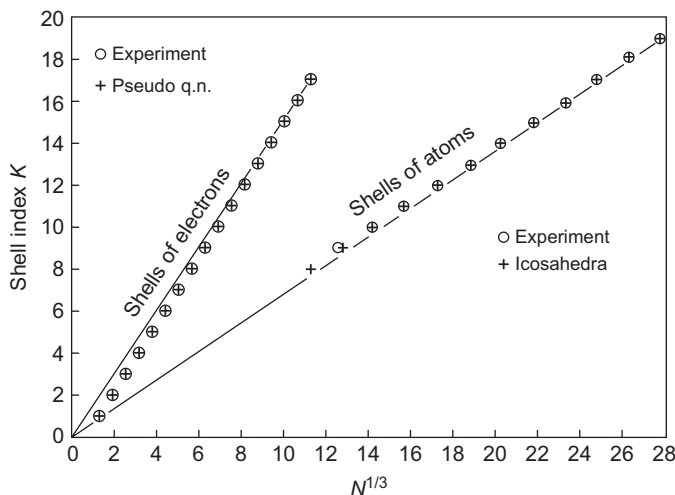


FIGURE 16.6

Shell index K plotted against $N^{1/3}$ for Na_N clusters.

Reproduced from Martin²⁵ with the permission of Elsevier.

16.3 GEOMETRIC SHELL STRUCTURE

16.3.1 Close-Packing

We have noted that for sodium clusters, for $N > 1500$, a new criterion for stability sets is based on the close-packing of atoms (the fcc or hcp structure in bulk) suitably modified by the presence of a surface. This is known as the geometric shell model. In fact, for other metallic clusters, the geometric shell model is the starting point for studies of stability and associated magic numbers. The bonding is dominated by the short-ranged $d-d$ interaction in metals such as nickel, and the configuration tends to maximize the number of nearest neighbors. The transition metals with unfilled d -shells have directional dependence in their bonding. An example is the bcc and hcp structure in bulk iron and cobalt atoms.

16.3.2 Wulff Construction

Wulff proposed that at equilibrium, the polyhedron is such that the perpendicular distance from the center of the particle to a face of the polyhedron is proportional to the surface energy of the face.³⁶ When one uses this procedure for a fcc metal, a polyhedron comprising eight (111) and six (100) faces, shown in Figure 16.7, is obtained. If one defines the perpendicular distance of the two faces as p_{111} and p_{100} , it can be shown that (Problem 16.4) the lengths of the sides of the faces are β and $(1-2\beta)$ in units of $\sqrt{6}p_{111}$, as shown in Figure 16.7. The scale factor β is given by

$$\beta = 1 - p_{100}/\sqrt{3}p_{111}. \quad (16.28)$$

If γ_{100} and γ_{111} are the surface energies of the two faces, we have from Eq. (16.28)

$$\beta = 1 - \frac{\gamma_{100}}{\sqrt{3}\gamma_{111}}. \quad (16.29)$$

Assuming pairwise interaction (ϕ) between nearest neighbors, the specific surface energy $\gamma = n_d\phi/A$, where n_d is the number of neighbors a surface atom is deficient, and A is the surface area per atom. An atom on the (100) surface has a deficiency of four neighbors compared with an atom in the bulk. Therefore,

$$\gamma_{100} = 4\phi/d^2, \quad (16.30)$$

where d is the nearest-neighbor distance. An atom on the (111) surface has nine neighbors and has a deficiency of three compared with an atom in the bulk. We thus have

$$\gamma_{111} = 2\sqrt{3}\phi/d^2. \quad (16.31)$$

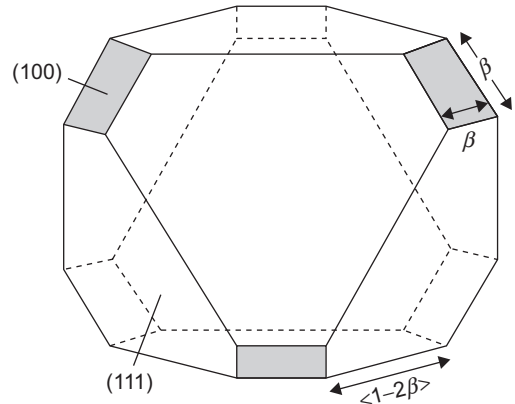


FIGURE 16.7

Polyhedral structure based on Wulff construction.

Reproduced from Marks (Ref. 24) with the permission of Elsevier.

From Eqs. (16.29) through (16.31), we obtain

$$\beta = \frac{1}{3}. \quad (16.32)$$

Thus, $\beta = 1 - 2\beta$ and, hence, the lengths of the sides of the hexagonal and square faces are equal. This is shown in Figure 16.8 for a 586-atom polyhedron. It may be noted that the Wulff criterion actually applies for large sizes when vertex and edge effects can be neglected.

16.3.3 Polyhedra

fcc

A basic shape that can be constructed from a symmetric cluster is the octahedron (see Figure 16.9) with eight triangular faces that are close-packed (111) planes with low surface energy.

In Figure 16.9, we defined a shell number K as the number of atoms along the edge of a face. A cluster with an even value of K is built around an elementary octahedron of six atoms while a cluster with an odd value of K has a single atom at its center. The total number of atoms N in a cluster containing K octahedral shells is

$$N = \frac{1}{3}(2K^3 + K). \quad (16.33)$$

A cuboctahedron, which is an octahedron truncated by a cube, was shown earlier in Figure 16.2. It has eight (111) and six square (100) faces. The polyhedron has a central atom and can be considered as built of successive shells covering interior shells. The K th shell contains $(10K^2 + 2)$ atoms. It can be shown that the total number of atoms in a cluster with K shells (Problem 16.5) is

$$N = \frac{1}{3}(10K^3 - 15K^2 + 11K - 3). \quad (16.34)$$

From Eq. (16.34), the magic numbers associated with geometric shell filling are 1, 13, 55, 147, 309, 561,

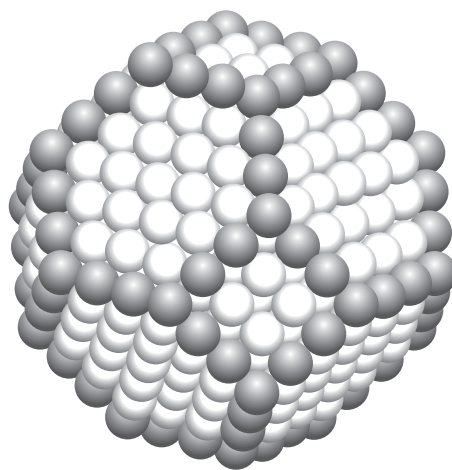


FIGURE 16.8

A 586-atom truncated octahedron with square and hexagonal faces.

Reproduced from Misra²⁸ with the permission of Elsevier.

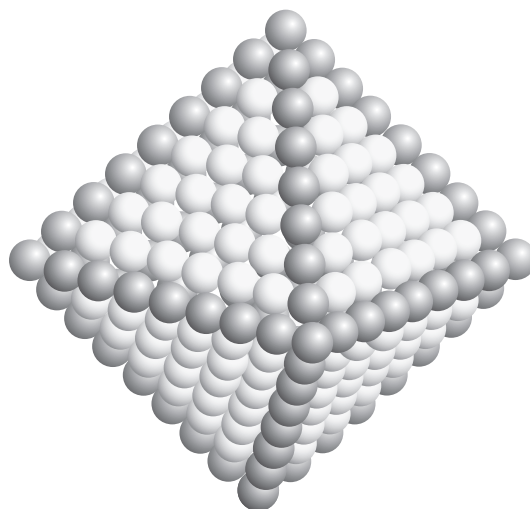


FIGURE 16.9

A 489-atom octahedron.

Reproduced from Misra²⁸ with the permission of Elsevier.

Mackay Icosahedron

It can be shown that the total surface energy can be minimized if all the faces of the polyhedron are (111) planes and the surface area can be kept at a minimum. The icosohedral structure shown in Figure 16.10a has 20 triangular faces and has this feature.

The Mackay icosahedron is made up of 20 distorted tetrahedra. The distortion is shown in Figure 16.10b. The vertex O is at the center (OA, OB, OC) are of unit length, the three sides of the equilateral triangle ABC are extended to 1.05146. The angles subtended at O are $63^\circ 26'$. The icosohedra can be constructed by arranging 12 neighbors of a central atom at the corners of an icosohedron. One can build larger clusters by covering the 13-atom core with a second layer of 42 atoms, a third of 92 atoms, and so on. The total number of atoms is identical to that of the cuboctahedron with triangular faces, as in Eq. (16.34). The reason for assignment of magic numbers to geometrical shell structures for large sodium clusters is that experimental results support the values from Eq. (16.34) with $K = 10$ –19, thereby confirming an icosohedral or cuboctahedral configuration. In addition, in the K against $N^{1/3}$ plots of Figure 16.6, there is a good fit to Eq. (16.36) in the large K limit (for $N > 1500$), whereas $N \approx 0.21 K^3$ fits for small clusters. One can show that the later equation can be obtained by using the Woods–Saxon potential.

bcc

The 369-atom rhombic dodecahedron shown in Figure 16.11 is one of the main cluster shapes based on the bcc lattice.

There are 12 identical faces of which the diagonals have lengths with the ratio $1:\sqrt{2}$, and this shape is similar to the cuboctahedron. The number of atoms, N , for a cluster of K shells is

$$N = 4K^3 - 6K^2 + 4K - 1. \quad (16.35)$$

Thus, the cluster sizes at successive shell fillings are 1, 15, 65, 369,

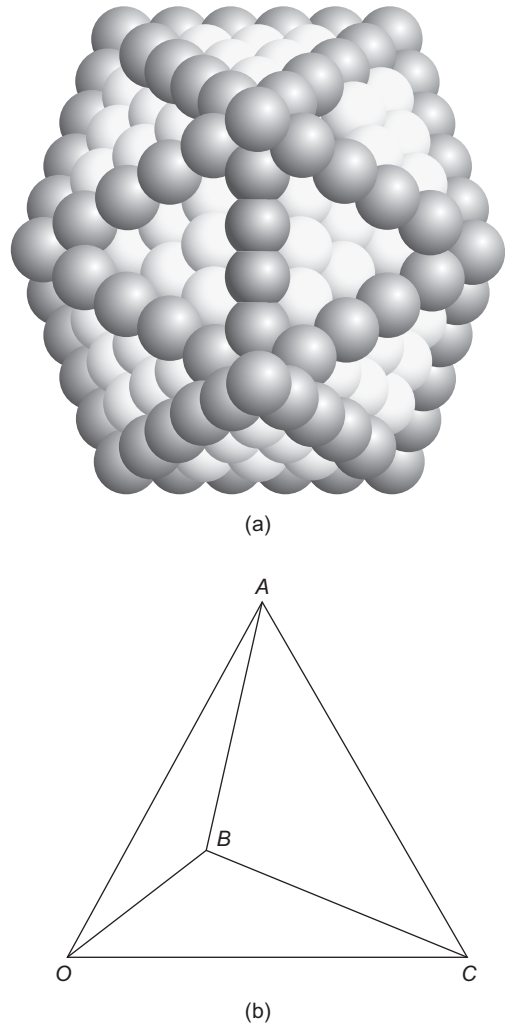
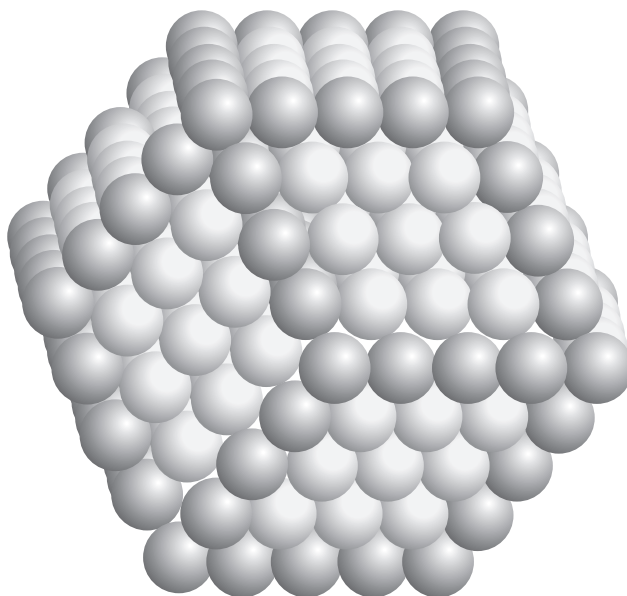


FIGURE 16.10

(a) An icosahedron of 561 atoms; (b) the Mackay icosahedron with vertex O at the center.

Reproduced from Misra²⁸ with the permission of Elsevier.

**FIGURE 16.11**

The 360-atom rhombic dodecahedron.

Reproduced from Misra²⁸ with the permission of Elsevier.

16.3.4 Filling between Complete Shells

There are two different models for filling of sub-shells in between the completion of the main shells of the Mackay (Ref. 21) icosohedra. In one model, one starts from a complete icosohedron and adds atoms that preferentially sit on the three-fold hollow formed by the three atoms on the (111) face, thereby maximizing their coordinate number. The atoms rearrange themselves to the Mackay packing arrangement when the shell is half filled. This model has been applied to rare-earth clusters. In the alternate model, also known as the umbrella model, the atoms are added to icosohedral sites on the surface of the core icosohedron. The covering of a complete face achieves enhanced stability.

16.4 CLUSTER GROWTH ON SURFACES

16.4.1 Monte Carlo Simulations

The easiest way to understand the key ideas of cluster growth on surfaces is through Monte Carlo simulation of cluster (or island) nucleation and growth during vapor deposition. Usually, through the use of a comprehensive set of simulations, an empty lattice is made to represent a substrate. The monomers are deposited at random into this lattice at a constant deposition rate. They can diffuse by random nearest-neighbor hops, and when they collide, they nucleate new point islands. The immobile islands “grow” whenever new monomers diffuse onto them. They remain as single points on the lattice while their recorded size increments by the number of adsorbed monomers. The

density of islands nucleated in the simulation depends on the ratio, R , of the monomer deposition rate to the monolayer deposition rate. R dictates the Monte Carlo simulation procedure, by changing the probabilities of the next simulation step being a deposition event or a monomer diffusion event. Typically, $R \sim 10^5 - 10^{10}$ in experimental growth conditions.

The Monte Carlo simulations throw up many questions relevant to experiment, such as (1) how does the island density depend on growth rate and temperature, (2) how does the critical island size i change with these conditions, (3) how does the island size distribution (ISD) depend on this critical island size, and (4) why it displays scale invariance?

16.4.2 Mean-Field Rate Equations

The following assumptions are made in deriving the mean-field rate equations:

- a. Only monomers are mobile.
- b. Islands of size $s \geq 2$ grow by capturing the diffusing monomers.
- c. Monomers are produced on the substrate by random deposition from vapor or by release from an existing island.
- d. The direct impingement from vapor onto existing monomers and islands can be neglected in the early stages of nucleation and growth.

The time evolution of monomer density N_1 and density N_s of islands of size s is

$$\frac{dN_1}{dt} = F - 2D\sigma_1 N_1^2 - DN_1 \sum_{s \geq 2} \sigma_s N_s + 2 \frac{N_2}{\tau_2} + \sum_{s \geq 3} \frac{N_s}{\tau_s} \quad (16.36)$$

and

$$\frac{dN_s}{dt} = DN_1 (\sigma_{s-1} N_{s-1} - \sigma_s N_s) + \frac{N_{s+1}}{\tau_{s+1}} - \frac{N_s}{\tau_s}. \quad (16.37)$$

Here, F is the monomer deposition rate (monolayer per second), D is the monomer diffusion rate, σ_s is the so-called “capture number” of monomers by an island of size s , and $1/\tau_s$ is the dissociation rate (rate of monomer release) of an island of size s .

The preceding equations can be numerically integrated up to some finite time and some maximum possible island size at that time, provided one knows σ_s , the capture numbers, and $1/\tau_s$, the dissociation rate of an island of size s . σ_s can be obtained by considering the monomer density $n_1(r, t)$ in the vicinity of a circular island of radius $r_s = \sqrt{s/\pi}$ at the origin and by using cylindrical symmetry. The monomer density is zero at the adsorbing island edge and rises to the global average N_1 a long way from the island. The diffusive flux into the island is given by

$$DN_1 \sigma_s = D 2\pi r_s \left. \frac{\partial n_1}{\partial r} \right|_{r_s}, \quad (16.38)$$

from which the capture number σ_s can be calculated. The monomer density field can be obtained from the diffusion equation by first assuming that the monomers can evaporate from the substrate at

the rate $1/\tau_a$ and that $N_1 \rightarrow F\tau_a$, a long way from the island. The later assumption implies that the density of islands is sufficiently low. The diffusion equation can be written as

$$\frac{\partial n_1(r, t)}{\partial t} = D\nabla^2 n_1(r, t) - \frac{n_1(r, t)}{\tau_a} + F. \quad (16.39)$$

In the steady state $t > \tau_a$, it can be shown from Eqs. (16.38) and (16.39) that the capture number σ_s can be written as (Problem 16.6)

$$\sigma_s = 2\pi X_s \frac{K_1(X_s)}{K_0(X_s)}, \quad (16.40)$$

where K_0 and K_1 are the Bessel functions and

$$X_s = \frac{r_s}{\sqrt{D\tau_a}}. \quad (16.41)$$

If we assume that the islands around the central one (being considered) are randomly distributed and each one has the same size $\langle s \rangle$ and the same capture number σ_x , τ_s in Eq. (16.40) can be replaced by τ such that

$$\frac{1}{\tau} = \frac{1}{\tau_a} + D\sigma_x N, \quad (16.42)$$

where $N = \sum_{s \geq 1} N_s$ is the density of stable islands. The evaporation of monomers can be switched off ($1/\tau_a = 0$) in Eq. (16.42) to model the “complete condensation” regime of the film growth.

In an improved method using the results from kinetic Monte Carlo simulations, it has been shown (Bales and Chazan¹) that a self-consistent solution for all σ_s can be used to reproduce the evolution of the monomer and total island density. In their work, Eq. (16.42) for the average capture number is replaced by

$$\frac{1}{\tau} = 2D\sigma_1 N_1 + \sum_{s \geq 2} D\sigma_s N_s + F\kappa_1, \quad (16.43)$$

which allows for monomer trappings by other monomers and direct hits from vapor deposition on existing monomers as well as capture by islands.

16.5 STRUCTURE OF ISOLATED CLUSTERS

16.5.1 Theoretical Models

Hartree–Fock Methods

The earliest method employed was the Hartree–Fock method (discussed in Chapter 4), but because it uses a single-determinant wave function, it does not describe electrons with different spins. The neglect of correlations produces energy values that are larger than the actual ones. There have been various methods used to include the effect of correlations in post-Hartree–Fock theories.

In the configuration interaction (CI) methods, one or more occupied orbitals in the Hartree–Fock determinant are replaced by virtual orbitals where each replacement is equivalent to an electron excitation. In the full CI method, the wave function is formed as a linear combination of the Hartree–Fock determinant and all possible substitute determinants. However, it is necessary to truncate the expansion at a fairly low level of substitution (single and double excitations) except for the smallest systems. There are refinements that use Rayleigh–Schrodinger perturbation theory and add the higher excitations as noniterative corrections. Usually, these methods are limited to small clusters of about 20 atoms.

Density Functional Theory

The local density approximation (LDA) in density functional theory (DFT) can be used by first writing the exchange–correlation energy as a sum of exchange and correlation part

$$E_{xc} = E_x + E_c. \quad (16.44)$$

If $\rho_\alpha(\mathbf{r})$ and $\rho_\beta(\mathbf{r})$ are the electron densities of the two spin components, ($\alpha = \uparrow$) and ($\beta = \downarrow$), the local exchange functional is given by the standard Dirac–Slater form

$$E_x^{LDA} = -\frac{3}{2} \left(\frac{3}{4\pi} \right)^{1/3} \int d\mathbf{r} [\rho_\alpha^{4/3} + \rho_\beta^{4/3}], \quad (16.45)$$

and the Kohn–Sham (Ref. 17) wave functions are atom-centered. The local spin-density correlation energy functional (Vosko et al.³⁴) can be written as

$$E_c^{LDA}[\rho_\alpha, \rho_\beta] = \int d\mathbf{r} \rho \varepsilon_c(\rho_\alpha, \rho_\beta), \quad (16.46)$$

where ε_c is a complicated function of ρ and several constants. However, the correlation energy is overestimated by 100% in this approximation.

A more widely used exchange–energy functional based on the generalized-gradient approximation (GGA) of Becke (Ref. 2) is given by

$$E_x^{GGA} = E_x^{LDA} - \beta \sum_{\sigma=\alpha,\beta} \int d\mathbf{r} \rho_\sigma^{4/3} \frac{x_\sigma^2}{1 + 6\beta x_\sigma \sinh^{-1}(x_\sigma)}, \quad (16.47)$$

where x_σ is the dimensionless ratio

$$x_\sigma = \rho_\sigma^{-4/3} |\nabla \rho_\sigma|. \quad (16.48)$$

In general, the GGA exchange–correlation energy functionals can be expressed as

$$E_{xc}^{GGA}[\rho_\uparrow, \rho_\downarrow] = \int d\mathbf{r} f(\rho_\uparrow, \rho_\downarrow, \nabla \rho_\uparrow, \nabla \rho_\downarrow). \quad (16.49)$$

An interesting technique to go beyond GGA is to use hybrid functionals that are formulated as a mixture of Hartree–Fock and DFT exchange coupled with DFT correlation. However, a number of authors have suggested that hybrid methods should be avoided for metal clusters because these techniques do not yield reliable results.

Tight-Binding Methods

The tight-binding model is used mainly in the study of transition metal clusters. The Hamiltonian is expressed in terms of matrix elements in an orthogonal basis set composed from the s , $p(x, y, z)$, $d(xy, yz, zx, x^2 - y^2, 3z^2 - r^2)$ valence atomic orbitals. The intersite matrix elements are determined by the Slater–Koster hopping integrals (Slater and Koster,³¹) $ss\sigma$, $sp\sigma$, $sd\sigma$, $pp\sigma$, $pd\pi$, $dd\delta$, which decay exponentially with distance, but the three-center integrals are ignored. In the model proposed by Mehl and Papaconstantopoulos,²⁷ the total energy is obtained by summing up the occupied energy levels,

$$\varepsilon_i = a_i + b_i \rho_i^{2/3} + c_i \rho_i^{4/3} + d_i \rho_i^2, \quad (16.50)$$

where

$$\rho_i = \sum_{j \neq i} \exp \left[-\gamma \left(\frac{r_{ij}}{r_0 - 1} \right) \right]. \quad (16.51)$$

The three on-site terms depend on the orbital angular momentum $\lambda = s, p, d$. In Eq. (16.51), r_0 is the interaction term in the bulk, and a cutoff is included in the distance in the sum. The repulsive energy is incorporated by varying it as a function of the total density of each function.

The Hamiltonian for the model is written as

$$H = \sum_{i\lambda\sigma} \varepsilon_{i\lambda} c_{i\lambda\sigma}^\dagger c_{i\lambda\sigma} + \sum_{\substack{i \neq j \\ \lambda\mu\sigma}} \beta_{ij}^{\lambda\mu} c_{i\lambda\sigma}^\dagger c_{j\mu\sigma}. \quad (16.52)$$

In Eq. (16.52), λ and μ are orbital labels, σ is the spin label, $\beta_{ij}^{\lambda\mu}$ are the hopping integrals between sites i and j , and the other symbols have their usual meanings. The different parameters are obtained by fitting to bulk properties. There are a large number of variations of the tight-binding model. Specifically, spin-polarized systems, a Hubbard-like term,

$$H_{\text{int}} = -\bar{J}_\lambda \sum_{i\lambda\sigma} \sigma c_{i\lambda\sigma}^\dagger c_{i\lambda\sigma}, \quad (16.53)$$

is added to Eq. (16.52). In Eq. (16.53),

$$\bar{J}_\lambda = \frac{1}{2} \sum_\mu J_{\lambda\mu} (\bar{n}_{i\mu\uparrow} - \bar{n}_{i\mu\downarrow}), \quad (16.54)$$

where $J_{\lambda\mu}$ is an exchange integral, and $\bar{n}_{i\mu\sigma}$ is the component of electron density at site i associated with orbitals μ and spin σ . A variety of additional terms are added to this basic model to obtain the computational results that can relate better to the cluster properties.

Semi-Empirical Potentials

To study large clusters, several semi-empirical potentials have been developed that contain many-body contributions and can be used with Monte Carlo or molecular dynamics simulations. The various models are known as embedded atom model (EAM), effective medium theory (EMT), glue

model, and second-moment methods. All these methods start with a common functional form for the total energy,

$$E = \sum_i \left[\frac{1}{2} \sum_{j \neq i} V(r_{ij}) + F(\bar{\rho}_i) \right], \quad (16.55)$$

where $\frac{1}{2} \sum_{j \neq i} V(r_{ij})$ is a repulsive pair potential between atoms separated by a distance r_{ij} . In the EAM (Daw and Baskes⁵; Foiles et al.¹⁰), each term of a metal is considered as an impurity embedded in a host provided by the rest of the electrons. $F(\bar{\rho}_i)$ is the energy required to embed atom i in an electron gas of density $\bar{\rho}_i$, where

$$\bar{\rho}_i = \sum_{j \neq i} \rho(r_{ij}). \quad (16.56)$$

One has to use empirical fits to bulk properties to be able to generate the embedding functions and pair interactions.

In the second-moment approximations (Finnis and Sinclair,⁹; Sutton,³³) the total energy is

$$E = \epsilon \sum_i \left[\sum_{j \neq i} V(r_{ij}) - c \sqrt{\rho_i} \right]. \quad (16.57)$$

One can see the similarity as well as the contrast between Eqs. (16.55) and (16.57). In Eq. (16.57), ϵ is a parameter that has dimensions of energy, and c is a dimensionless parameter. ρ_i is expressed as a sum of pair potentials

$$\rho_i = \sum_{j \neq i} \phi(r_{ij}). \quad (16.58)$$

ρ_i can be described as the bond energy. We consider just one orbital site and local density of states $d_i(E)$ at site i with a center of gravity ϵ_i . The bond energy is given by

$$E_{bond} = 2 \sum_i \int_{-\infty}^{E_F} (E - \epsilon_i) d_i(E) dE. \quad (16.59)$$

The second moment of the local density of states can be written as

$$\mu_i^{(2)} = \int_{-\infty}^{\infty} (E - \epsilon_i)^2 d_i(E) dE. \quad (16.60)$$

From Eqs. (16.59) and (16.60), we obtain an approximation in which moments no higher than the second are used (Problem 16.7),

$$E_{bond}^{(i)} = A \sqrt{\mu_i^{(2)}}, \quad (16.61)$$

where A is a constant. It can be shown that the local density of states can be written as

$$d_i(E) = \langle i | \delta(E - H) | i \rangle, \quad (16.62)$$

where H is the Hamiltonian for the system, and $|i\rangle$ is the orbital on-site i . From Eqs. (16.60) and (16.62), we obtain an expression for the second moment,

$$\begin{aligned} \mu_i^{(2)} &= \int_{-\infty}^{\infty} (E - \varepsilon_i)^2 \langle i | \delta(E - H) | i \rangle dE \\ &= \langle i | (\varepsilon_i - H)^2 | i \rangle. \end{aligned} \quad (16.63)$$

We can write the Hamiltonian H as

$$H = \sum_i \varepsilon_i |i\rangle \langle i| + \sum_{i \neq j} \beta_{ij} |i\rangle \langle j|, \quad (16.64)$$

where ε_i is the energy at site i , and β_{ij} is the hopping integral from site i to j . From Eqs. (16.63) and (16.64), we obtain

$$\mu_i^{(2)} = \sum_{j \neq i} \beta_{ij}^2. \quad (16.65)$$

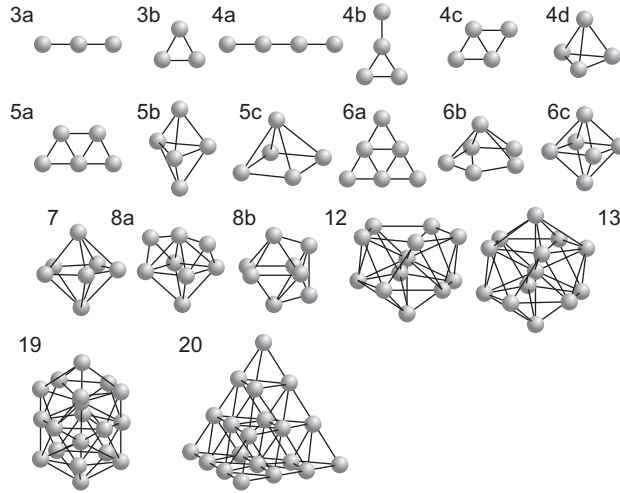
The second-moment approximation is very effective for metals that tend to form close-packed structures. However, one needs the fourth moment, which controls the stability of the bcc structure, and the fifth and sixth moments if hcp and fcc packing are to be differentiated. There are several other semi-empirical potentials that we will not discuss in this chapter.

There are several alternate models to choose the potential in Eqs. (16.57) and (16.58). Once a potential is chosen, there are many global optimization techniques that can be used to find the lowest energy of a cluster. The standard Monte Carlo or molecular dynamics procedure is used after incorporating some algorithms. The computation involved is very massive, but fairly good global minima have been obtained for clusters of more than 100 atoms.

16.5.2 Structure of Some Isolated Clusters

A schematic configuration of a number of commonly occurring small clusters is shown in Figure 16.12. There is usually some departure from the symmetric configurations shown in the figure. The linear and planar clusters usually show some departure from one or two dimensionality, and triangular configuration in 3b is isosceles instead of equilateral. The three-dimensional clusters occur at various sizes. One extreme is nickel, which has a tetrahedral structure at $N = 4$, whereas the other extreme is gold clusters, which are planar until $N > 10$. The alkali metals are between these two extremes. An interesting aspect is that anions and cations have different structures than neutral clusters.

A large number of experimental research is focused on probing clusters of special sizes to verify whether magic number clusters, such as icosahedral or cuboctahedral (13, 55, 147), truncated octahedral (38), or Marks decahedral (75, 146, 192), are more stable than clusters of other sizes as suggested by the geometrical shell model.

**FIGURE 16.12**

Schematic representation of some small clusters. The 3D figures are (4d) tetrahedron, (5b) trigonal bipyramid, (5c) square pyramid, (6b) pentagonal pyramid, (6c) octahedron, (7) pentagonal bipyramid, (8a) bicapped octahedron, (8b) bisphenoid, (12) incomplete icosahedron, (13) icosahedron, (19) double icosahedron, and (20) large tetrahedron.

Reproduced from Misra²⁸ with the permission of Elsevier.

16.6 MAGNETISM IN CLUSTERS

16.6.1 Magnetism in Isolated Clusters

Superparamagnetism and Blocking Temperature

There has been a rapidly growing interest in the nanostructures formed from magnetic clusters because of their enormous potential in the development of high-performance magnetic materials and devices. There has been considerable development of technologies in the manufacture of quantum dots, monolayers, self-organized islands, quantum wires, and deposited nanoclusters. However, magnetism in small clusters, which is in the mesoscopic regime, is not well understood in either the atomic or bulk states.

It has been shown (Skomski,³⁰) that nanoclusters are single-domain particles of which the size is well below the critical radius R_{SD} , above which it is favorable to form domain walls. For a sphere,

$$R_{SD} = \frac{36\sqrt{AK}}{\mu_0 M_s^2}, \quad (16.66)$$

where M_s is the spontaneous magnetization, K is an anisotropy constant, and A is related to the exchange stiffness.

At low temperatures (well below the equivalent of the Curie temperature), the nanoparticles can be considered as giant magnetic moments of ferromagnetically coupled spins. This phenomenon is

known as superparamagnetism. In an external field, the reorientation of this giant moment takes place coherently and the individual moments remain aligned with each other. The different magnetic alignments are separated by an anisotropy boundary KV , where V is the volume of the nanoparticle and K is the anisotropic constant. At high temperatures, because $k_B T \gg KV$, the anisotropic boundary becomes unimportant, but there is a competition between the external field, which tends to orient the particles, and the thermal fluctuations of the magnetic moments, which tend to magnetically disorder the array.

The volume V of the transition metal clusters is $V \leq 10^{-25} \text{ m}^3$, and at room temperature, $k_B T \gg KV$. Because all magnetization directions have equal probability, the magnetization M of a cluster along the direction of an applied field H can be obtained from the classical Langevin function L ,

$$M = \mu_c \mathcal{L}\left(\frac{\mu_c H}{k_B T}\right), \quad (16.67)$$

where μ_c is the giant magnetic moment of each cluster and $\mathcal{L}(x) = \coth(x) - 1/x$.

An assembly of nanoclusters, each of which has several hundred atomic spins, can be easily saturated, unlike an assembly of atoms. At temperatures less than 50° K , $k_B T \sim KV$, and the magnetization in a given field deviates from superparamagnetism. At very low temperatures, the moment in each particle becomes static. The blocking T_B is the temperature at which half the cluster moments have relaxed during the time of a measurement. Because a narrow temperature region around T_B separates the frozen moments from superparamagnetic behavior, these can be used in magnetic recording technology provided one can obtain deposited small clusters with T_B greater than the room temperature. In fact, the deposition of clusters or their embedding in a matrix is essential for practical applications.

Cluster Magnetism

The magnetism in small clusters is usually significantly different from bulk magnetism of the same atoms because a much larger percentage of atoms in a cluster lies at the surface. For example, 162 of the atoms in a 309-atom cuboctahedral cluster lie at the surface, and these atoms have a reduced coordination and are in a lower symmetry environment. In the second-moment approximation discussed earlier, the bandwidth W is proportional to $z^{1/2}$, where z is the coordination number. For simplicity, if we consider a rectangular band for the d electrons, the density of states scales as $1/W$ (Problem 16.8).

The reduced coordination of the surface atoms results in an enhanced density of states $D(\epsilon_F)$. We have derived in Eq. (13.111),

$$M \approx \frac{2\mu_B^2 B D(\epsilon_F)}{1 - U D(\epsilon_F)}. \quad (16.68)$$

Thus, due to the Stoner criterion for ferromagnetic instability, $U D(\epsilon_F) > 1$, there is possibility of ferromagnetic instability in clusters that was absent in the bulk material.

The reduced z_i , the coordination number of the surface atoms, will result in an increase of the local moments μ_i on the atom i on the surface compared with the bulk value μ_{bulk} .

A crude approximation is

$$\mu_i = \left(\frac{z_{bulk}}{z_i} \right)^{1/2} \mu_{bulk}. \quad (16.69)$$

However, a reduced coordination in the second-moment approximation causes a contraction in the interatomic distances, which reduces the magnetic moment. A simple expression proposed for the average moment $\bar{\mu}_N$ of a cluster of N atoms (Jensen and Bennemann,¹⁴) is given by

$$\mu_N = \mu_{bulk} + (\mu_{surf} - \mu_{bulk})N^{-1/3}. \quad (16.70)$$

The experiments indicate a more complex size dependence but confirm the trend of the decrease in moment toward the bulk value with increasing size.

16.6.2 Experimental Techniques for Studying Cluster Magnetism

Chemical Probe Methods

The chemical probe method is usually used to investigate the geometric structure of clusters of Fe, Co, and Ni (and other transition metals) up to the sizes of 200 atoms. Atoms and small molecules react with transition metal clusters in ways that are analogous to the physisorption and chemisorption processes that occur on metal surfaces. The geometric structure of the cluster can be inferred from the fact that the reactivity of the cluster is dependent on the environment of the atoms. The main probe molecules that have been used are NH_3 , N_2 , H_2O , and H_2 or D_2 . The determination of the number of binding sites of a cluster for a particular molecule yields important clues as to possible structures. Because the d -orbitals have significant spatial extent and are involved in the transition metal bonding, the chemical properties are sensitive to both the number and the configuration of the d electrons.

The experimental arrangement is as follows. The clusters are produced by a pulsed laser vaporization of a metal target in a flow tube upstream of a flow-tube reactor (FTR) using helium gas. To ensure that the cluster growth is finished and clusters have cooled to ambient temperature before they enter the FTR, one uses a narrow flow tube and low helium pressure to ensure a rapid decrease in metal atom density. The reagent gas is introduced when the clusters enter the FTR. The reaction between the cluster, M_N , and the reagent molecule, A , produces an internally excited complex,



The excited complex requires a collision with a third body (a carrier gas atom, C) to stabilize it,



The clusters and reaction products expand out of the nozzle and form into a molecular beam. The clusters are then pulsed laser ionized and mass analyzed in a time-of-flight mass spectrometer. There are different binding rules for the various reagent molecules. Surface studies indicate that the NH_3 molecule binds to the surface through the donation of the N -localized lone pair to a metal atom. However, in the case of clusters, the binding preferentially occurs on the low-coordination metal atoms, which means that saturation with ammonia counts the number of vertex atoms on a

FIGURE 16.13

Comparison of structures of 3–19 atom nickel and cobalt structures.

Reproduced from Riley²⁹ with the permission of Elsevier.

Gradient-Field Deflection (Stern–Gerlach)

The gradient-field deflection method is based on the classic Stern-Gerlach experiment that first detected the electron spin. A schematic diagram of the experiment for measuring the magnetic moment of free clusters is shown in Figure 16.14.

A collimated cluster beam that is generated by a pulsed laser evaporation source with a variable temperature nozzle is guided into a magnetic field gradient dB/dz , which deflects a particle of magnetic moment M vertically by

$$d = M \frac{dB}{dz} L^2 \frac{(2D/L + 1)}{2mv_x^2}. \quad (16.73)$$

Here, m is the mass of the cluster, and v_x is its velocity when it enters the magnet. D is the distance from the end of the magnet of length L to the detector. v_x is measured by a controlled delay between the evaporation laser and the ionizing laser. A mechanical chopper is used in front of the source to define the pulse start time. Figure 16.15 shows the low-temperature total moments of Fe_N , Co_N , and Ni_N (in μ_B/atom) as a function of cluster size. The right scale in Figure 16.15 indicates the spin imbalance obtained from the equation

$$\frac{M_{\text{spin}}}{M_{\text{tot}}} = \frac{2}{g}, \quad (16.74)$$

where g is the gyromagnetic ratio.

One can see in Figure 16.15 that clusters with different sizes show locked-moment behavior. The moment of the Ni cluster drops rapidly to the bulk value at $N = 160$ and then increases slowly until it reaches the bulk value again at $N \approx 350$. The moments of Fe and Co clusters fall less rapidly. They reach the bulk value between $N \approx 400$ –500.

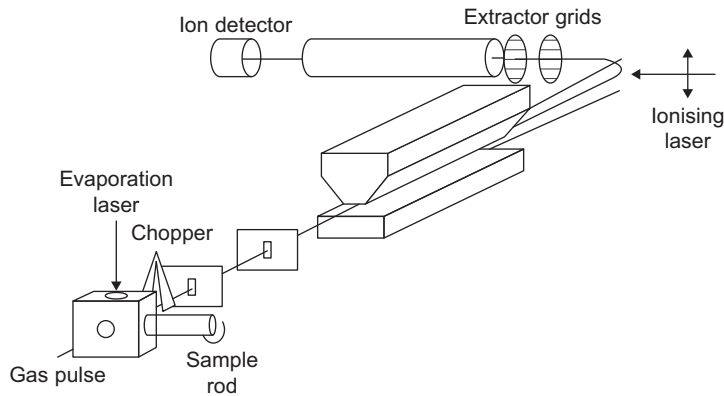
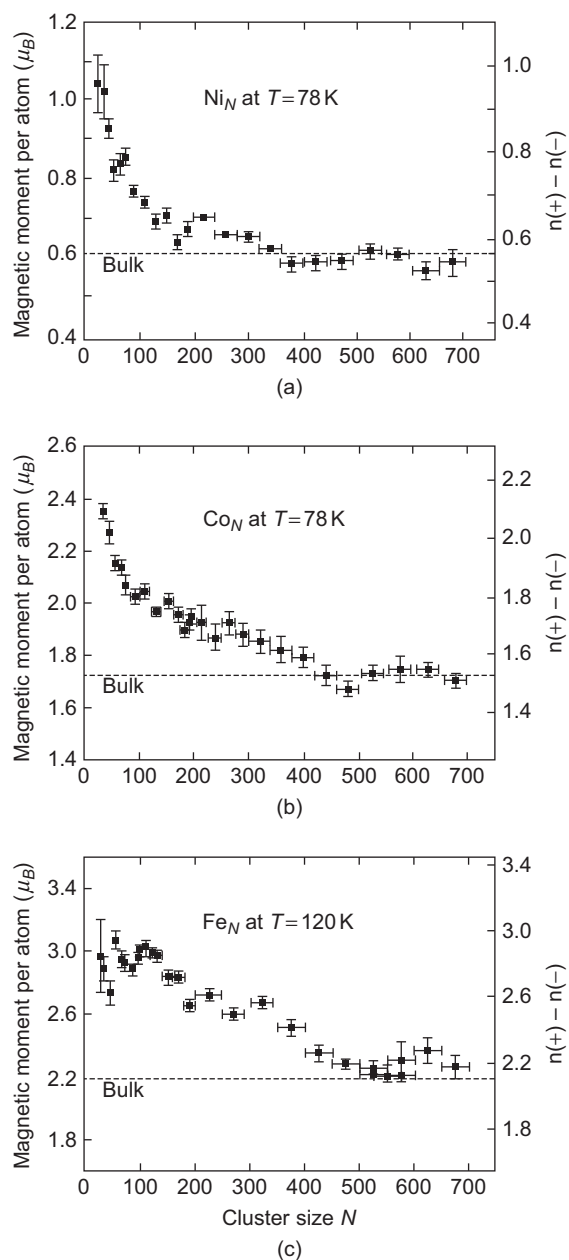


FIGURE 16.14

Schematic of the experiment for measuring the magnetic moment of free clusters.

Reproduced from Misra²⁸ with the permission of Elsevier.

**FIGURE 16.15**

Low-temperature total moments (in μ_B/atom) of (a) Ni_N , (b) Co_N , and (c) Fe_N . The right scale indicates the spin imbalance defined in Eq. (16.74).

Reproduced from Isabella et al.¹³ with the permission of Elsevier.

The magnetic behavior of clusters primarily depends on their structure. Most of the theoretical work has been done using density functional theory and geometry optimization; however, the details of the theoretical calculations are beyond the scope of this book.

16.6.3 Magnetism in Embedded Clusters

Switching and Blocking Temperature

The interest in magnetic nanoparticles has recently increased considerably because of the device applications such as in ultra-high-density recording as well as in spintronics. For device applications, the nanoclusters are either deposited on a surface or embedded in another material. The embedding material can modify the properties of the magnetic clusters to a great extent.

Switching (from magnetism to superparamagnetism) is a major factor in miniaturization of devices. When the energy barrier due to anisotropy, KV , becomes very small, the probability of switching due to the thermal energy becomes significant, which creates problems in such devices. The probability, P , of not switching in time t is given by the Boltzmann statistics

$$P = e^{-\frac{t}{\tau}}, \quad (16.75)$$

and the Arrhenius relation

$$\frac{1}{\tau} = f_0 e^{-\left(\frac{KV}{k_B T}\right)}, \quad (16.76)$$

where f_0 is the attempt frequency. The blocking temperature, which marks the onset of instability during an observation time τ , is obtained from Eq. (16.76) as

$$T_B = \frac{KV}{k_B \ln(f_0 \tau)}. \quad (16.77)$$

For a spherical particle of diameter D , $V = 1/6 \pi D^3$, and from Eq. (16.77), we obtain

$$T_B = \frac{\pi K D^3}{6 k_B \ln(f_0 \tau)}. \quad (16.78)$$

For data storage, the time constant $\tau \approx 10$ years, which yields $\ln(f_0 \tau) \approx 40$. For a typical uniaxial anisotropy $K \approx 0.2 \text{ MJ/m}^3$, and Eq. (16.77) yields for a nanocluster with $D = 14 \text{ nm}$, $T \approx 520^\circ \text{ K}$ for a 10-year blocking temperature, which is well above the operating temperature of a memory device. However, for a nanocluster for which $D = 7 \text{ nm}$, $T \approx 65^\circ \text{ K}$, which is far lower than the room temperature.

One option to increase the blocking temperature is to increase the anisotropy K by depositing ferromagnetic particles on a platinum surface (which has large spin-orbit interaction) or the formation of alloys such as CoPt or FePt. An alternate approach to increase the effective anisotropy is through relying on the exchange bias phenomenon. This is based on the enhanced stability of the ferromagnetic component due to the exchange coupling at the interface of a ferromagnetic and anti-ferromagnetic material as well as the high anisotropy in the antiferromagnet.

Small Clusters and 2D Nanostructures

In this section, we first study the introduction of small 3d metal clusters on surfaces of a noble metal (Cu(001)). The results of the calculations are based on density functional theory and the KKR method in which a Green's function technique is used to treat the perturbation of a surface into the ideal crystal and then placing an adatom or cluster on the surface. Figure 16.16 shows the spin magnetic moment of 3d metal clusters and monolayer on Cu(001).

One can note that the moments on the Co and Fe atoms plotted in Figure 16.16 are relatively insensitive to the island size.

The deposition of atoms of the 3d elements onto a ferromagnetic surface shows that the magnetic moments of the adatoms may align parallel or antiparallel to the direction of magnetization of the substrate. There is further complexity with 2d clusters or nanolayers if there is a tendency for antiferromagnetic ordering within the nanostructure itself. The spin magnetic moments obtained from using KKR Green's function method with exchange and correlation effects on monolayers on bcc Fe(001) are shown in Figure 16.17.

Similar results have been obtained for fcc Ni(001) substrate except for Mn. The total energy calculations for fcc Ni(001) substrate on Mn indicate ferromagnetic coupling for all positions. Further, the enhancement of the impurity moments is larger with Ni(001) than with Fe(001) because the hybridization is weaker due to the fact that the Ni wave function is less extended. The dimers on next-nearest-neighbor sites on top of Fe(001) couple to the surface with the same configuration as the adatoms except for Mn. The moments of the dimer atoms are parallel to each other. However, for the Mn dimer, the two states are energetically degenerate, one with the moments on both atoms ferromagnetically coupled to the substrate, whereas the other has the moments of the dimer atoms antiparallel.

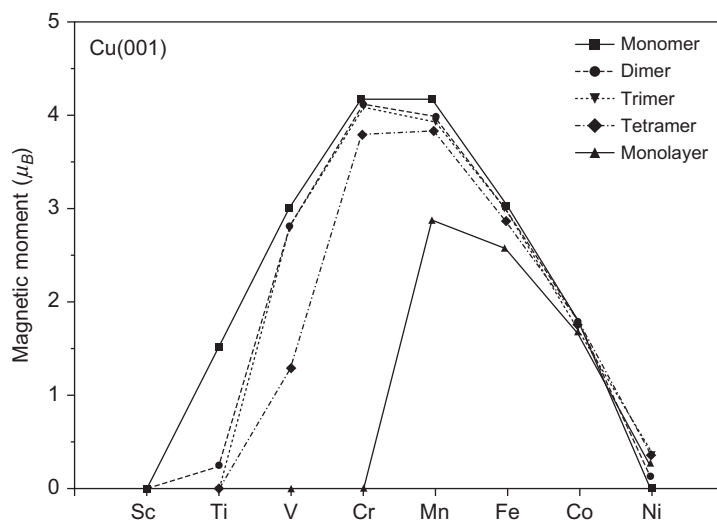


FIGURE 16.16

Spin magnetic moment of 3d metal clusters and monolayer on Cu(001).

Reproduced from Stepanyuk et al.³² with the permission of Elsevier.

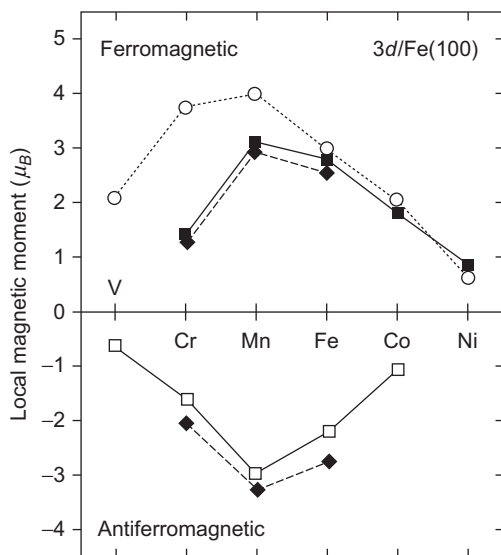


FIGURE 16.17

Magnetic moments of the monolayer on the surface: p(1 x 1) ferromagnetic coupling (solid squares/solid line); layered antiferromagnetically (open squares); c(2 x 2) ferromagnetic (diamonds/dashed line); 3d monolayers on Ag(001) for comparison.

Reproduced from Handschuh and Blugel¹¹ with the permission of Elsevier.

moments of $N = 2-9$ Fe clusters on Ni(001), which adopt a planar geometry on top of the Ni(001) surface, have spin moments that vary smoothly from $3.15 \mu_B$ to $2.85 \mu_B$ for $N = 2$ to $N = 9$ (Martinez et al.²⁶). In contrast, the experimental results (Lau et al.²⁰) indicate oscillations. These contradictory results are shown in Figure 16.18.

16.6.4 Graphite Surfaces

The spin magnetic moments of the 3d transition metal adatoms and dimers on a graphite surface from the calculations of Duffy and Blackman⁶ and of 3d monolayers by Kruger et al. (Ref. 19) are shown in Figure 16.19.

16.6.5 Study of Clusters by Scanning Tunneling Microscope

The ability to image single impurity atoms on a surface by scanning tunneling microscope (STM) has become very convenient to study the properties of clusters on the surface of a metal. The images of magnetic atoms on the surface of a metal and the Kondo resonance can be obtained from the current versus voltage characteristics. STM experiments measure the bias voltage dependence of

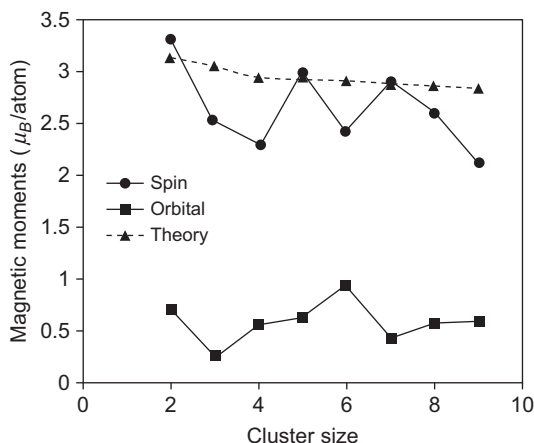


FIGURE 16.18

Experimental results from Lau et al.¹⁵ of spin and orbital moments (in μ_B/atom) and theoretical results from Martinez et al.²⁶ for spin moments for Fe clusters deposited on Ni/Cu (001) clusters.

Reproduced from Misra²⁸ with the permission of Elsevier.

It is interesting to note that the spin moments of Fe clusters deposited on the Ni(001) surface are enhanced compared with bulk bcc Fe. The results of theoretical calculation, using a modified embedded atom model, show that the spin

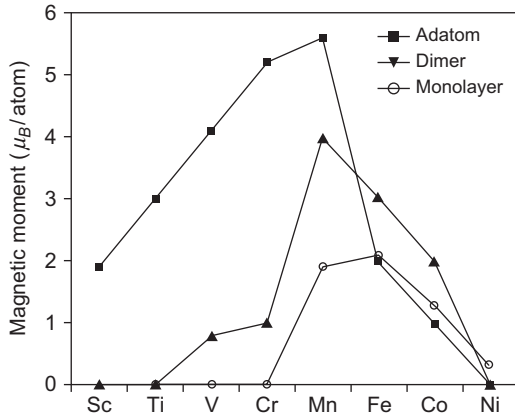


FIGURE 16.19

Composite showing the results of calculations of spin moments of 3d transition metal adatoms, dimers (Duffy and Blackman,⁶ and monolayers (Kruger et al.¹⁹) on graphite. The Mn monolayer has antiferromagnetic and ferrimagnetic ground states that are degenerate.

Reproduced from Misra²⁸ with the permission of Elsevier.

the differential conductance dI/dV . The electrons tunnel between states at ε_F on the tip and states at $\varepsilon_F + eV$ on the surface, so the structure in the measured differential conductance reflects the surface density of states at that energy. Because the STM probes a localized state immersed in a Fermi sea, the spectroscopy is that of a discrete auto-ionized state. We discuss the case of noninteracting impurity resonances that have no Coulomb interactions. This is the situation when the s -orbital of an adatom hybridizes with a metal surface. Such a system can be described by a resonant-level model, where the electron is allowed to hop between the discrete atomic orbital and the continuum of the electronic band states. Thus, the Kondo resonance can be analyzed as a type of Fano resonance (Fano,⁸). Fano showed that the Hamiltonian for a discrete state and a continuum, ignoring the spin, can be written as

$$\hat{H}_0 = \sum_{\mathbf{k}} \varepsilon_{\mathbf{k}} \hat{c}_{\mathbf{k}}^\dagger \hat{c}_{\mathbf{k}} + \varepsilon_a \hat{a}^\dagger \hat{a} + \sum_{\mathbf{k}} (V_{a\mathbf{k}} \hat{a}^\dagger \hat{c}_{\mathbf{k}} + V_{a\mathbf{k}}^* \hat{c}_{\mathbf{k}}^\dagger \hat{a}), \quad (16.79)$$

where ε_a , \hat{a}^\dagger , and \hat{a} are, respectively, the energy, creation, and annihilation operators of an electron residing in the discrete atomic state; and $V_{a\mathbf{k}}$ is the hybridization matrix element connecting the atomic state to the k th band state. The advanced atomic-state Green's function can be written as (Madhavan et al.²³)

$$G_{aa}^0(\varepsilon) = \frac{1}{\varepsilon - [\varepsilon_a + [\text{Re } \Sigma_0(\varepsilon) + i \text{Im } \Sigma_0(\varepsilon)]]}, \quad (16.80)$$

where the real and imaginary parts of the self-energy are

$$\text{Re } \Sigma_0(\varepsilon) = \sum_{\mathbf{k}} |V_{a\mathbf{k}}|^2 P\left(\frac{1}{\varepsilon - \varepsilon_{\mathbf{k}}}\right) \quad (16.81)$$

and

$$\text{Im } \Sigma_0(\varepsilon) = \pi \sum_{\mathbf{k}} |V_{a\mathbf{k}}|^2 \delta(\varepsilon - \varepsilon_{\mathbf{k}}). \quad (16.82)$$

Here, P denotes the Cauchy principal value. In the context of STM, the energy $\varepsilon = eV$.

In a tunneling experiment, a second electrode (the tip) is added to the system, and electrons tunnel between the electrodes. The tip is modeled by a single state with energy ε_t , and \hat{t} removes an electron from that state. \hat{M} is a transfer Hamiltonian term (treated as a perturbation) that induces electrons to tunnel from one electrode to the other and can be expressed as

$$\hat{M} = (M_{at} \hat{a}^\dagger \hat{t} + H.c.) + \sum_{\mathbf{k}} (M_{kt} \hat{c}_{\mathbf{k}}^\dagger \hat{t} + H.c.). \quad (16.83)$$

M_{at} and M_{kt} are the tunnel matrix elements that connect the STM tip to the discrete atomic state and continuum states, respectively. From Eqs. (16.79) and (16.83), we obtain

$$\hat{H} = \hat{H}_o + \hat{e}_t \hat{t}^\dagger \hat{t} + \hat{M}. \quad (16.84)$$

It can be shown that the differential conductance can be written as (Problem 16.9)

$$\frac{dI}{dV} = \frac{2\pi e^2}{\hbar} \frac{(\epsilon' + q)^2}{1 + \epsilon'^2} \rho_{\text{tip}} \sum_{\mathbf{k}} |M_{\mathbf{k}t}|^2 \delta(eV - \epsilon_{\mathbf{k}}) + \text{constant}, \quad (16.85)$$

where

$$q = A/B, \quad (16.86)$$

$$A = M_{at} + \sum_{\mathbf{k}} M_{\mathbf{k}t} V_{a\mathbf{k}} P\left(\frac{1}{eV - \epsilon_{\mathbf{k}}}\right), \quad (16.87)$$

$$B = \pi \sum_{\mathbf{k}} M_{\mathbf{k}t} V_{a\mathbf{k}} \delta(eV - \epsilon_{\mathbf{k}}), \quad (16.88)$$

$$\epsilon' = \frac{eV - \epsilon_a - \text{Re} \Sigma(eV)}{\text{Im} \Sigma(eV)}, \quad (16.89)$$

and ρ_{tip} is the tip density of states. ρ_{tip} is usually treated as a constant to reflect the broadening of the tip state by contact with the remainder of the tip electrode. Here, the quantity A in Eq. (16.87) is an amplitude for tunneling to the discrete state modified by hybridization with the continuum (the second term in Eq. 16.87). The quantity B in Eq. (16.88) is an amplitude for tunneling into a set of continuum states contained in the range of energies on the order of the width of the resonance. If $q \gg 1$, tunneling via the resonance dominates, but if $q \ll 1$, the continuum states dominate the tunneling.

The experimental results for Co atoms on the Au(111) substrate are reproduced in Figure 16.20. This figure shows how the dI/dV spectra vary as the STM tip is moved with a clear feature of the intermediate q type appearing when the tip is in the vicinity of the Co atom, indicating Kondo resonance.

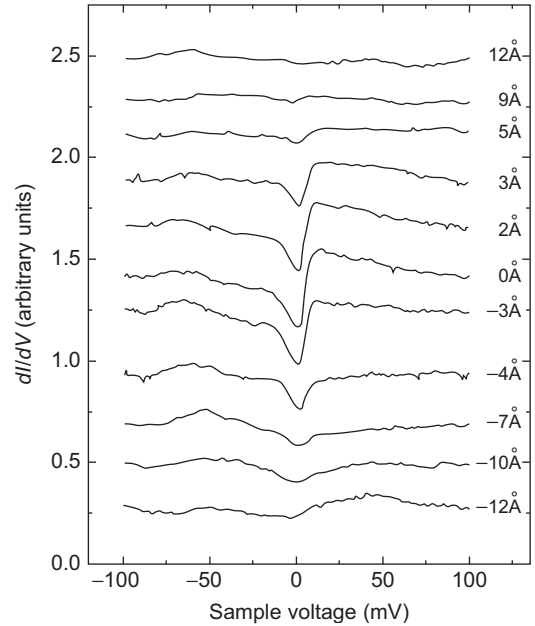


FIGURE 16.20

dI/dV spectra at various lateral distances away from the center of a single Co atom on Au(111) taken with the STM tip.

Reproduced from Madhavan et al.²² with the permission of AAAS.

16.6.6 Clusters Embedded in a Matrix

The magnetic properties of particles are modified when they are embedded in a matrix of another material. The magnetic moment of a

free particle is enhanced over the bulk value because the coordination of the atoms at the surface of the particle is reduced. In contrast, the embedded particle has the coordination of its surface atoms restored. The probability of the magnetic moment reverting to its bulk value depends on the electronic band structures of the particle and the host matrix. Further, if the particle and the matrix have the same bulk crystal structure with similar lattice spacings, there is the possibility of embedding with fairly good epitaxy. In contrast, if the two materials have different structures, the particle structure could either remain robust or adapt to that of the host matrix.

The overall picture for the full concentration range can be visualized by considering the magnetic phase diagram for films of deposited 3 nm diameter Fe nanoparticles embedded in Ag matrices, as shown in Figure 16.21.

Ideal superparamagnetism occurs at the lowest concentrations above a blocking temperature. When the volume filling fraction (VFF) increases, the magnetic behavior is determined by the dipolar interactions and the aggregation. A correlated superspin glass (CSSG) state occurs at higher concentrations. Blocking occurs at low temperatures, and the particles are aligned to their anisotropy axes. There is a significant difference between single-particle blocking and collective blocking. The single-particle blocking occurs in isolated clusters because the intraparticle anisotropy is the only characteristic to stabilize the magnetic moment. Strong interparticle interactions lead to collective blocking, which occurs at higher temperatures. Collective blocking occurs due to the fact that a particle, which would be thermally activated if it was isolated, would have its magnetization stabilized by a neighbor that is slightly larger or more anisotropic.

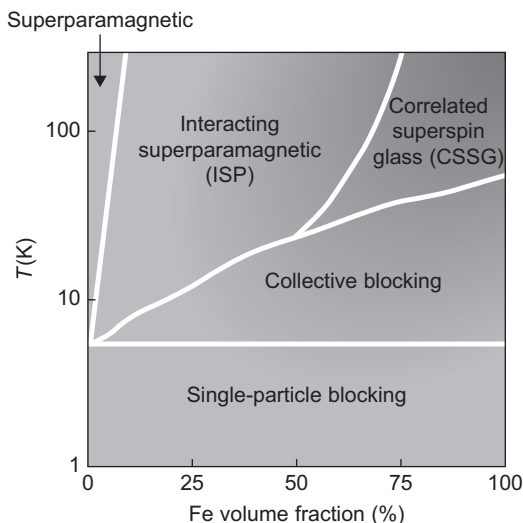


FIGURE 16.21

Magnetic phase diagram for films of deposited 3 nm diameter Fe nanoparticles embedded in Ag matrices as a function of volume fraction and temperature.

Reproduced from Binns et al.³ with the permission of the Institute of Physics.

16.7 SUPERCONDUCTING STATE OF NANOCCLUSERS

16.7.1 Qualitative Analysis

In Chapter 14, expressions for the critical temperature T_c in both the weak coupling (BCS) and the strong coupling (McMillan) theories were derived. The expression for the critical temperature T_c in the weak-coupling limit (Eq. 14.116) is

$$T_c \approx 1.13 \theta_D \exp \left[-\frac{2}{D(\epsilon_F)U} \right], \quad (16.90)$$

and in the strong coupling limit (Eq. 14.127), it is

$$T_c \approx \frac{\theta_D}{1.2} \exp \left[-\frac{1.04(1+\lambda)}{\lambda - \mu^*(1+0.62\lambda)} \right]. \quad (16.91)$$

In Eq. (16.91), λ is the coupling constant (Eq. 14.124),

$$\lambda = \nu < I^2 > / M \bar{\Omega}^2, \quad (16.92)$$

and ν is the bulk density of states (Eq. 14.125),

$$\nu = m^* p_F / 2\pi^2. \quad (16.93)$$

It is obvious from Eqs. (16.90) and (16.91) that T_c , the critical temperature of a superconductor, increases if the density of states increases at the Fermi level. In fact, it has been observed that the T_c of Al films ($\sim 2.1^\circ \text{K}$) is nearly double the value for bulk samples. Granular Al has $T_c \sim 3^\circ \text{K}$, which is almost three times the critical temperature of Al. These increases were explained by size quantization and corresponding increase in the effective density of states in films and isolated granules.

The metallic nanoclusters contain delocalized electrons of which the states organize into shells, similar to those in atoms or nuclei. In some clusters, the shells are completely filled all the way up to the highest occupied shell. These are known as the “magic numbers,” $N = N_m = 20, 40, 58, 92, 138, 168, \dots$, and the clusters are spherical. These magic clusters have similarity with atoms in the sense that their electronic states are labeled by radial quantum number n and orbital momentum l . The Cooper pairs are formed by electrons with opposite projections of orbital momentum, similar to the pairing in atomic nuclei. The degeneracy of the shell, which is $2(2l+1)$, is large if l is large, and the effective density of states correspondingly increases. Further, the energy spacing ΔE between neighboring shells varies. Some of them are separated by only a small ΔE .

The combination of high degeneracy and a small energy spacing ΔE between the highest occupied shell (HOS) and the lowest unoccupied shell (LUS) results in a large increase in the strength of the superconducting pairing interaction in the clusters. One can understand this result qualitatively from the fact that if the HOS is highly degenerate, the shell has a large number of electrons, which is equivalent to having a sharp peak in the density of states at the Fermi level. It is obvious from Eqs. (16.90) and (16.91) that the critical temperature of a superconductor increases if the density of states increases at the Fermi level.

16.7.2 Thermodynamic Green's Function Formalism for Nanoclusters

In this section, we will derive an expression for the critical temperature for the nanoclusters. We will show how it is possible that the critical temperature for some of these nanoclusters can be of the order of room temperature. We follow a method outlined by Kresin and Wolf.¹⁸ However, we will not discuss in detail the strong coupling theory based on Green's function method of the many-body theory.

In the standard thermodynamic Green's function formalism of Abrikosov et al. (1963), the equation for the pairing order parameter, $\Delta(\omega)$, can be written as

$$\Delta(\omega_n)Z \approx \lambda T \sum_{\omega_{n'}} D(\omega_n - \omega_{n'}; \tilde{\Omega}) F^+(\omega_{n'}), \quad (16.94)$$

where Z is the renormalization function that describes the “dressing” of electrons moving through the lattice, λ is the electron–phonon coupling constant,

$$\lambda = 2 \int \alpha^2(\Omega) F(\Omega) \Omega^{-1} d\Omega, \quad (16.95)$$

$F(\Omega)$ is the phonon density of states, Ω is the phonon frequency, and $\alpha^2(\Omega)$ is a measure of the phonon-frequency-dependent electron–phonon interaction. Here, D is the phonon Green’s function,

$$D = \Omega^2 [(\omega_n - \omega_{n'})^2 + \Omega^2]^{-1}, \quad (16.96)$$

where

$$\omega_n = (2n + 1)\pi T \quad (16.97)$$

and

$$\tilde{\Omega} = \langle \Omega^2 \rangle^{1/2}. \quad (16.98)$$

The average $\langle f(\Omega) \rangle$ is determined by

$$\langle f(\Omega) \rangle = \frac{2}{\lambda} \int d\Omega f(\Omega) \alpha^2(\Omega) F(\Omega) \Omega^{-1}, \quad (16.99)$$

and the pairing Green’s function, introduced by Gorkov, is given by

$$F^+ = \Delta(\omega_n) / [\omega_n^2 + \xi^2 + \Delta^2(\omega_n)]. \quad (16.100)$$

In Eq. (16.100), ξ is the electron energy relative to the chemical potential. The metallic clusters contain delocalized electrons of which the states organize into shells. For some clusters that are spherical, the shells are filled up to the highest occupied shell, i.e., those with the magic numbers $N = N_m = 20, 40, 58, 92, 138, 168, \dots$. The electronic states in the magic clusters are labeled by radial quantum number n and orbital momentum l . The Cooper pairs are formed by electrons with opposite projections of orbital momentum, and if the orbital momentum is large, the shell has a degeneracy of $2(2l + 1)$.

For nanoclusters, of volume V , Eqs. (16.92), (16.93), (16.94), (16.96), and (16.100) are modified as

$$\Delta(\omega_n) Z = \eta \frac{T}{2V} \sum_{\omega_{n'}} \sum_s D(\omega_n - \omega_{n'}, \tilde{\Omega}) F_s^+(\omega_{n'}), \quad (16.101)$$

where

$$\eta = \langle I^2 \rangle / M \tilde{\Omega}^2, \quad (16.102)$$

$$D(\omega_n - \omega_{n'}, \tilde{\Omega}) = \tilde{\Omega}^2 [(\omega_n - \omega_{n'})^2 + \tilde{\Omega}^2]^{-1}, \quad (16.103)$$

$$F_s^+(\omega_{n'}) = \Delta(\omega_{n'}) [\omega_{n'}^2 + \xi_s^2 + \Delta^2(\omega_{n'})]^{-1}, \quad (16.104)$$

and

$$\xi_s = E_s - \mu. \quad (16.105)$$

Here D and $F_s^+(\omega_n)$ are the vibrational propagator and the pairing function, $\Delta(\omega_n)$ is the order parameter, Z is the renormalization function, E_s is the energy of the s th electronic state, and μ is the chemical potential. The summation is over all the discrete electronic states. There are two aspects in which these equations differ from the corresponding equations for the bulk. First, they contain a summation over discrete energy levels E_s instead of integration over a continuous energy spectrum, as in a bulk superconductor. Second, because the number of electrons is fixed, the position of the chemical potential μ is determined by N and T and hence different from the value of Fermi level E_F .

Kresin and Wolf (Ref. 18) also showed that because “magic clusters” have a spherical shape, one can replace the summation over states by summation over shells $\Sigma_s \rightarrow \sum_j G_j$, where G_j is the shell degeneracy

$$G_j = 2(2l_j + 1), \quad (16.106)$$

and l_j is the orbital momentum. They showed that for such clusters, Eqs. (16.101) through (16.104) can be written in the form

$$\Delta(\omega_n)Z = \lambda \frac{2E_F}{3N} \sum_{\omega_n} \sum_j G_j \frac{\tilde{\Omega}^2}{\tilde{\Omega}^2 + (\omega_n - \omega_{n'})^2} \frac{\Delta^2(\omega_{n'})}{\omega_{n'}^2 + \xi_l^2} |T_c. \quad (16.107)$$

In Eq. (16.107), the bulk coupling constant λ (Eq. 16.92) and the Fermi energy E_F are used because the characteristic vibrational frequency is close to the bulk value due to the fact that the pairing is mediated mostly by the short-wave part of the vibrational spectrum.

However, if the shell is incomplete, there is a Jahn–Teller deformation in the cluster. Because the shape becomes ellipsoidal, the s states are classified by their projection of the orbital momentum $|m| \leq l$, and each level contains up to four electrons for $|m| \geq 1$. In the weak coupling case, $\eta/V \ll 1$, which leads to $\pi T_c \ll \tilde{\Omega}$. In Eqs. (16.101), (16.103), and (16.104), one should substitute $Z = 1$ and $D = 1$. This leads to the BCS (weak coupling) theory.

It may be noted that Eqs. (16.101), (16.103), and (16.104) are different from the strong-coupling theory of bulk superconductors in two aspects. First, they contain a summation over discrete energy levels E_s , whereas one integrates over a continuous energy spectrum (over ξ) in bulk superconductors. Second, because the clusters have a finite Fermi system, the number of electrons N is fixed. Hence, the position of the chemical potential μ is different from the Fermi level E_F and is determined by the value of N and T .

The value of the critical temperature T_c in a nanocluster depends on the number of valence electrons N ; the energy spacing $\Delta E = E_L - E_H$; and on the values of λ_b , E_F , and $\tilde{\Omega}$. One can obtain a high value of T_c (as high as 100° K) by using realistic values of these parameters.

The pairing in an isolated cluster can be observed from the strong temperature dependence of the excitation spectrum. When $T \sim 0^\circ$ K, the excitation energy is strongly modified by the gap parameter and significantly exceeds the gap parameter when $T > T_c$. For example, the minimum absorption energy for Gd₈₃ clusters at $T > T_c$ corresponds to $\hbar\omega \approx 6$ meV, whereas for $T \ll T_c$, its value is much larger: $\hbar\omega \approx 34$ meV.

Recently, Cao et al.⁴ measured the heat capacity of an isolated cluster. They observed a jump in heat capacity for selected Al clusters (i.e., for Al₃₅⁺ ions) at $T \approx 200^\circ$ K. The value of T_c as well as the amplitude of the jump and its width are in agreement with this theory.

PROBLEMS

16.1. We have shown that for a metallic cluster, the total energy can be written as

$$E[n] = E_k[n] + E_{es}[n] + E_{xc}[n], \quad (1)$$

where $E_k[n]$ is the kinetic energy of a system of independent particles of density n ,

$$E_k[n] = \sum_i \frac{\hbar^2}{2m} |\nabla \psi_i|^2. \quad (2)$$

$E_{es}[n]$ is the electrostatic energy,

$$E_{es}[n] = \frac{e^2}{2} \iint d\mathbf{r}' d\mathbf{r} \frac{[n(\mathbf{r}) - n_I(\mathbf{r})][n(\mathbf{r}') - n_I(\mathbf{r}')]}{|\mathbf{r} - \mathbf{r}'|}, \quad (3)$$

and $E_{xc}[n]$ is the exchange-correlation term of the energy. Following the procedure outlined in Section 7.8.2 (subject to the modification for a metallic cluster), show that

$$-\frac{\hbar^2}{2m} \nabla^2 \psi_i(\mathbf{r}) + V_{KS}(\mathbf{r}) \psi_i(\mathbf{r}) = \varepsilon_i \psi_i(\mathbf{r}), \quad (4)$$

where

$$V_{KS}(\mathbf{r}) = V_H(\mathbf{r}) + V_{xc}(\mathbf{r}), \quad (5)$$

$$V_H(\mathbf{r}) = 2e^2 \int d\mathbf{r}' \frac{n(\mathbf{r}') - n_I(\mathbf{r}')}{|\mathbf{r} - \mathbf{r}'|}, \quad (6)$$

and

$$V_{xc}(\mathbf{r}) = \frac{\partial \varepsilon_{xc}(n)}{\partial n} \varepsilon_{xc}(n) \quad (7)$$

Here, $\varepsilon_{xc}(n)$ is the exchange-correlation energy of the electron gas.

16.2. Show that in Eq. (16.24),

$$\langle l^2 \rangle_n = \left(\frac{1}{2} \right) n(n+3). \quad (1)$$

16.3. The ellipsoidal model is based on the harmonic oscillator Hamiltonian

$$H = \frac{p^2}{2m} + \frac{1}{2} m \omega_0^2 [\Omega_\perp^2 (x^2 + y^2) + \Omega_z^2 z^2] - U \hbar \omega_0 [l^2 - \langle l^2 \rangle_n]. \quad (1)$$

Ignoring the anharmonic terms in Eq. (1), show that

$$E(n_1, n_2, n_3) = \hbar \omega_0 \left[\Omega_\perp (n_1 + n_2 + 1) + \Omega_z \left(n_3 + \frac{1}{2} \right) \right]. \quad (2)$$

By using the definition of the distortion parameter defined in the text,

$$\delta = \frac{2(\Omega_{\perp} - \Omega_z)}{\Omega_{\perp} + \Omega_z}, \quad (3)$$

show that Eq. (2) can be written as

$$E(n_1, n_2, n_3) = \hbar\omega_0 \left[n + \frac{3}{2} + \frac{\delta}{3}(n - 3n_3) + \frac{\delta^2}{18}(n + 3n_3 + 3) \right], \quad (4)$$

where

$$n = n_1 + n_2 + n_3. \quad (5)$$

- 16.4.** If one defines the perpendicular distance of the two faces as p_{111} and p_{100} , show that the lengths of the sides of the faces of the Wulff polyhedron (Figure 16.7) are β and $(1 - 2\beta)$ in units of $\sqrt{6}p_{111}$. The scale factor β is given by $\beta = 1 - p_{100}/\sqrt{3}p_{111}$.
- 16.5.** The polyhedron has a central atom and can be considered as built of successive shells covering interior shells. The K th shell contains $(10K^2 + 2)$ atoms. Show that the total number of atoms in a cluster with K shells is

$$N = \frac{1}{3}(10K^3 - 15K^2 + 11K - 3). \quad (1)$$

- 16.6.** The diffusive flux into the island is given by

$$DN_1\sigma_s = D2\pi r_s \frac{\partial n_1}{\partial r} \Big|_{r_s}, \quad (1)$$

from which the capture number σ_s can be calculated. The monomer density field can be obtained from the diffusion equation by first assuming that the monomers can evaporate from the substrate at the rate $1/\tau_a$ and that $N_1 \rightarrow F\tau_a$, a long way from the island. The latter assumption implies that the density of islands is sufficiently low. The diffusion equation can be written as

$$\frac{\partial n_1(r, t)}{\partial t} = D\nabla^2 n_1(r, t) - \frac{n_1(r, t)}{\tau_a} + F. \quad (2)$$

In the steady state $t > \tau_a$, which can be shown from Eqs. (1) and (2), show that the capture number σ_s can be written as

$$\sigma_s = 2\pi X_s \frac{K_1(X_s)}{K_0(X_s)}, \quad (3)$$

where K_0 and K_1 are the Bessel functions and

$$X_s = \frac{r_s}{\sqrt{D\tau_a}}. \quad (4)$$

- 16.7.** We considered the simple case of one orbital site and local density of states $d_i(E)$ at site i with center of gravity $d_i(E)$,

$$E_{bond} = 2 \sum_i \int_{-\infty}^{E_F} (E - \varepsilon_i) d_i(E) dE. \quad (1)$$

The second moment of the local density of states can be written as

$$\mu_i^{(2)} = \int_{-\infty}^{\infty} (E - \varepsilon_i)^2 d_i(E) dE. \quad (2)$$

We represent $d_i(E)$ by a Gaussian centered at ε_i and at width $\sqrt{\mu_i^{(2)}}$. By invoking the condition of charge neutrality to confirm that other factors arising out of Gaussian integration of Eq. (1) are site-independent, show that, in an approximation in which moments no higher than the second are used, the bond energy $E_{bond}^{(i)}$ is given by

$$E_{bond}^{(i)} = A \sqrt{\mu_i^{(2)}}, \quad (3)$$

where A is a constant.

- 16.8.** In the second-moment approximation discussed earlier, show that the bandwidth W is proportional to $z^{1/2}$, where z is the coordination number. For simplicity, if we consider a rectangular band for the d electrons, show that the density of states scales as $1/W$.
- 16.9.** Show that the low-temperature STM differential conductivity can be written as

$$\frac{dI}{dV} = \frac{2\pi e^2}{\hbar} \frac{(\varepsilon' + q)^2}{1 + \varepsilon'^2} \rho_{tip} \sum_{\mathbf{k}} |M_{\mathbf{k}l}|^2 \delta(eV - \varepsilon_{\mathbf{k}}) + \text{constant}, \quad (1)$$

where

$$q = A/B, \quad (2)$$

$$A = M_{at} + \sum_{\mathbf{k}} M_{\mathbf{k}l} V_{a\mathbf{k}} P \left(\frac{1}{eV - \varepsilon_{\mathbf{k}}} \right), \quad (3)$$

$$B = \pi \sum_{\mathbf{k}} M_{\mathbf{k}l} V_{a\mathbf{k}} \delta(eV - \varepsilon_{\mathbf{k}}), \quad (4)$$

$$\varepsilon' = \frac{eV - \varepsilon_a - \text{Re} \Sigma(eV)}{\text{Im} \Sigma(eV)}, \quad (5)$$

and ρ_{tip} is the tip density of states. ρ_{tip} is usually treated as a constant to reflect the broadening of the tip state by contact with the remainder of the tip electrode. (Hint: Most of the derivation is outlined in the appendix of the research paper by Madhavan et al.²³).

References

1. Bales GL, Chrazan DC. Dynamics of irreversible growth during submonolayer epitaxy. *Phys Rev B* 1994;**50**:6057.
2. Becke AD. Density-functional exchange energy approximation with correct asymptotic behavior. *Phys. Rev. A* 1988;**38**:3098.
3. Binns C, Trohidou KN, Bansmann J, Baker SH, Blackman J, Bucher J-P, et al. The behaviour of nonstructured magnetic materials produced by depositing gas-phase nanoparticles. *J Phys D: Appl Phys* 2005;**38**:R357.
4. Cao B, Neal CN, Starace AK, Ovchinnikov YN, Kresin V, et al. Evidence of of High-Tc Superconducting Transition in Isolated Al 45- and Al 47- isolated nanoclusters. *J Supercond Novel Magn* 2008;**21**:163.
5. Daw MS, Baskes MI. Embedded-atom method: Derivation and application to impurities, surfaces and other defects in metals. *Phys Rev B* 1984;**29**:6443.
6. Duffy D, Blackman JA. The energy of Ag adatoms and dimers on graphite. *Surf Sci* 1998;**415**:L1016.
7. Ekardt W. Work function of small metal particles: Self-consistent spherical jellium background model. *Phys Rev B* 1984;**29**:1558.
8. Fano U. Effects of Configuration Interaction on Intersites and Phase Shifts. *Phys Rev* 1961;**124**:1866.
9. Finnis MW, Sinclair JE. A simple empirical potential for transition metals. *Philos Mag A* 1984;**50**:45.
10. Foiles SM, Baskes MI, Daw MS. Embedded-atom-method functions for the fcc metals Cu, Ag, Au, Ni, Pd, Pt, and their alloys. *Phys Rev B* 1986;**33**:7983.
11. Handschuh S, Blugel S. Magnetic Exchange Coupling of 3d metal monolayers on Fe(001). *Solid State Commun.* 1998;**108**:633.
12. Hohenberg P, Kohn W. Inhomogeneous electron gas. *Phys Rev B* 1970;**1**:4555.
13. Isabelle M, Billas L, de Heer WA. Magnetism of Fe, Co, Ni clusters in molecular beams. *J. Magn. Magn. Mater.* 1997;**168**:64.
14. Jensen PD, Bennemann KH. A simple empirical N-body potential for transition metals. *Z Phys D* 1995;**35**:273.
15. Katakuse IT, Ichihara Y, Fujita Y, Matsuo T, Sakurai T, Matsuda H. Correaltion between mass distribution of zinc, cadmium cluster and electronic shell structure. *Int J Mass Spectr Ion Processes* 1986; **69**:109.
16. Knight WD, Clemenger K, de Heer WA, Saunders WA, Chou MY, Cohen ML. Electroanic Shell Structures and Abundance of Sodium Cluster. *Phys Rev Lett* 1984;**52**:2141.
17. Kohn W, Sham LJ. Self-consistent Equations Including Exchange and Correlation effects. *Phys Rev* 1965;**140**:A 1133.
18. Kresin VZ, Wolff SA. Electron-lattice interaction and its impact on high Tc superconductivity. *Rev Mod Phys* 2009;**81**:481.
19. Kruger P, Rakoatomahevitra A, Parbelas JC, Demangeat C. Magnetism of eptaxial 3d-transition-metal monolayers on graphite. *Phys Rev B* 1998;**57**:5276.
20. Lau JT, Fohllisch A, Martins M, Nietubyc, Reif M, Wurth W. Spin and orbital magnetic moments of deposited small iron clusters studied by X-ray magnetic circular dichroism spectroscopy. *New J Phys* 2002;**4**:98.
21. Mackay AL. A dense non-crystallograohic packing of equal spheres. *Acta Crystallogr* 1962;**15**:916.
22. Madhavan V, Chen W, Jameneala J, Crommie MF, Wingreen NS. Tunneling into a single Magnetic Atom: Spectroscopic Evidence of the Kondo Resonance. *Science* 1998;**280**:567.
23. Madhavan V, Chen W, Jameneala J, Crommie MF, Wingreen NS. Local Spectroscopy of a Kondo impurity: Co on Au(111). *Phys Rev B* 2001;**64**:165412.
24. Marks LD. Modified Wulff construction for twinned particles. *J. Cryst. Growth* 1983;**61**:556.
25. Martin TP. Shells of Atoms. *Phys Rep* 1984;**273**:199.
26. Martinez E, Lange RC, Robles R, Vega A, Gallgo LJ. Structure and magnetic properties of small Fe clusters supported on the Ni (001) surface. *Phys Rev* 2005;**71**:165424.

27. Mehl MJ, Papaconstantopoulos DA. Applications of a tight-binding total-energy method for transition and noble metals: Elastic constants, vacancies and surfaces of monatomic metals. *Phys Rev B* 1996;**54**:4519.
28. Misra PK, series editor, Blackman J, editor. *Metallic Nanoparticles*. Amsterdam: Elsevier; 2009.
29. Riley SJ. The atomic structure of transition metal clusters. *J Non-Cryst Solids* 1996;**205–207**:781.
30. Skomski R. Nanomagnetism. *J Phys Condens Matter* 2003;**15**:R 841.
31. Slater JC, Koster GF. Simplified LCAO Method for the Periodic Potential Problem. *Phys Rev* 1954;**94**:1498.
32. Stepanyuk VS, Hergert A, Rennert P, Wildberger K, Zeller R, Dedelichs PA. Transition metal magnetic nanostructures on metal surfaces. *Surface Sci* 1997;**377–379**:495.
33. Sutton AP. *Electronic Structure of Materials*. Oxford: Oxford University Press; 1993.
34. Vosko SJ, Wilk L, Nusair M. Accurate spin-dependent electron liquid correlation energies for local spin density calculations: a critical analysis. *Can J Phys* 1980;**58**:1200.
35. Woods BD, Saxon DS. Diffuse Surface Optical Mode for Nucleon-Nucleon Scattering. *Phys Rev* 1954;**95**:577.
36. Wulff G. *Z Krist* 1901;**34**:449.